*J. Fluid Mech.* (2011), *vol.* 680, *pp.* 602–635. 
doi:10.1017/jfm.2011.198

# The spatial distribution of gyrotactic swimming micro-organisms in laminar flow fields

R. N. BEARON[1]†, A. L. HAZEL[2] AND G. J. THORN[3]

[1]Department of Mathematical Sciences, University of Liverpool, Liverpool L69 7ZL, UK

[2]School of Mathematics, University of Manchester, Manchester M13 9PL, UK

[3]School of Mathematical Sciences, University of Nottingham, Nottingham NG7 2RD, UK

(Received 22 March 2010; revised 18 November 2010; accepted 29 April 2011; first published online 13 June 2011)

We compare the results of two-dimensional, biased random walk models of individual swimming micro-organisms with advection–diffusion models for the whole population. In particular, we consider the influence of the local flow environment (gyrotaxis) on the resulting motion. In unidirectional flows, the results of the individual and population models are generally in good agreement, even in flows in which the cells can experience a range of shear environments, and both models successfully predict the phenomena of gravitactic focusing. Numerical results are also compared with asymptotic expressions for weak and strong shear. Discrepancies between the models arise in two cases: (i) when reflective boundary conditions change the orientation distribution in the random walk model from that predicted by the long-term asymptotics used to derive the advection–diffusion model; (ii) when the spatial and temporal scales are not large enough for the advection–diffusion model to apply. We also use a simple two-dimensional flow containing a variety of flow regimes to explore what happens when there are localized regions in which the generalized Taylor dispersion theory used in the derivation of the population model does not apply. For spherical cells, we find good agreement between the models outside the 'break-down' regions, but comparison of the results within these regions is complicated by the presence of nearby boundaries and their influence on the random walk model. In contrast, for rod-shaped cells which are reorientated by both vorticity and strain, we see qualitatively different spatial patterns between individual and advection–diffusion models even in the absence of gyrotaxis, because cells are advected between regions of differing rates of strain.

**Key words:** micro-organism dynamics, suspensions

## 1. Introduction

Swimming micro-organisms are ubiquitous in fluid environments. Phytoplankton in particular are important in a wide variety of natural phenomena. These single-celled organisms, many of which are motile, are integral players in the oceanic ecosystem. For example, massive phytoplankton blooms can have major economic and environmental impact (Horner, Garrison & Plumley 1997). In the context of climate change, the oceans are among the largest sinks of carbon dioxide (Raven & Falkowski 1999), which is transformed by phytoplankton into organic carbon, providing food for a

† Email address for correspondence: rbearon@liv.ac.uk

wide range of organisms; from marine bacteria which recycle carbon from lysed phytoplankton, to blue whales which sieve the phytoplankton from the water.

The spatial distribution of phytoplankton in the natural environment is heterogeneous. For example, thin layers of phytoplankton have been observed *in situ* (e.g. Sharples *et al.* 2001; McManus *et al.* 2003; Steinbuck *et al.* 2009) and attempts have been made to explain these through physical and biological mechanisms alone (e.g. Franks 1995; Birch, Young & Franks 2008), and including the effect of swimming (Bearon, Grünbaum & Cattolico 2006; Durham, Kessler & Stocker 2009). On smaller scales, the phenomenon of bioconvection provides visually striking evidence of how swimming can interact with fluid dynamics to generate spatial patterns (see review by Hill & Pedley 2005). Understanding the fundamental differences between how actively swimming micro-organisms disperse in flow compared to passive solutes also has industrial relevance, for example in the design of bioreactors, which has recently received renewed interest within the context of bio-fuel production (Bees & Croze 2010).

Here, we focus on gyrotactic phytoplankton; single-celled bottom-heavy organisms that tend to swim upwards in still fluid but are reorientated from the vertical in shear flow because of viscous torques (Pedley & Kessler 1992). Our focus will be on dilute suspensions of these organisms, in that we neglect cell–cell interactions. This is motivated by the observation that cells can typically be cultured in liquid suspensions to a maximum volume fraction of only $10^{-3}$. We note however that the effect of actively swimming cell–cell interactions on the collective motions and fluid rheology of a suspension is an area of active study, recently reviewed by Ishikawa (2009).

In a still fluid, the swimming behaviour of individual gyrotactic phytoplankton can be described as a biased random walk: the cell orientation is assumed to be a random variable that undergoes diffusion with drift (Hill & Häder 1997). At the population level, the dynamics can be modelled by an advection–diffusion equation for the cell concentration, $n(\boldsymbol{x}, t)$, where the advection coefficient is the mean-swimming velocity of the cells and the anisotropic diffusion tensor represents the random component of swimming (Bearon & Grünbaum 2008).

Ambient fluid motion will interact with the swimming behaviour and alter the spatial distribution of a population. For example, suppose a cell is subject to a uniform external field which acts to align cells in the direction of the unit vector $\boldsymbol{F}$. Phytoplankton are typically sufficiently small and slow moving such that the local fluid dynamics are governed by the equations of Stokes flow and it can be assumed that there is no net torque on the cell. Under these conditions, a general ambient flow affects the orientation of an axi-symmetric cell via the local vorticity $\boldsymbol{\omega}$ and local rate of strain tensor $\boldsymbol{E}$, and the cell will rotate according to the deterministic formula

$$\dot{\boldsymbol{p}} = \frac{1}{2B}[\boldsymbol{F} - (\boldsymbol{F}\cdot\boldsymbol{p})\boldsymbol{p}] + \frac{1}{2}\boldsymbol{\omega}\wedge\boldsymbol{p} + \alpha_0\boldsymbol{p}\cdot\boldsymbol{E}\cdot(\boldsymbol{I} - \boldsymbol{p}\boldsymbol{p}), \tag{1.1}$$

where $\boldsymbol{p}$ is the swimming direction, $B$ is a time scale for the cell to reorient towards $\boldsymbol{F}$ and $\alpha_0$ is a measure of cell non-sphericity, termed the Bretherton constant, with $\alpha_0 = 0$ for a sphere and $\alpha_0 = 1$ for an infinitely thin rod (Pedley & Kessler 1992; Kim & Karrila 2005). In addition, the fluid flow itself will be affected by the presence of the cells, but we shall neglect any such feedback in the current work.

Dynamical systems methods combined with individual-based simulations have provided insight into the transport and spatial distribution of self-propelled particles advected by an externally imposed flow. For example, Torney & Neufeld (2007) demonstrated in two dimensions the aggregation of thin rod-like particles in laminar

flow, and Thorn & Bearon (2010) investigated the transport and dispersion of spherical gyrotactic organisms in a range of three-dimensional flows.

The orientation distribution of cells subject to viscous and gravitational torques and rotational diffusion was computed by Bees, Hill & Pedley (1998) and Almog & Frankel (1998) for unbounded homogeneous shear flow. Given the orientation distribution, it is simple to calculate the mean-swimming velocity of the cells, but the resultant diffusion tensor is more complicated. For homogeneous shear flow, with the additional constraint that eigenvalues of the fluid velocity gradient tensor have zero real part (see § 2.2.1 for further details), Hill & Bees (2002) and Manela & Frankel (2003) calculated expressions for the diffusion tensor using the theory of generalized Taylor dispersion (Frankel & Brenner 1991, 1993).

To model phytoplankton in the natural turbulent environment or more well-defined situations such as bioconvection, a population-level model is needed that describes the spatial distribution of the cells in an arbitrary flow field. Manela & Frankel (2003) suggest that the theory of generalized Taylor dispersion, valid for homogeneous shear flow, is suitable for bioconvection because the velocity gradient varies on length and time scales that are large relative to the microscopic relaxation in orientation space. However, the slowly swimming cells may be rapidly advected through the flow field, and so may experience rapidly changing shear. Furthermore, in bioconvection, there may be regions of the flow field where the eigenvalues of the fluid velocity gradient tensor do not have zero real part and thus the theory of generalized Taylor dispersion may not apply. A main motivation for the research presented here is to investigate whether the advection–diffusion population-level model derived from the theory of generalized Taylor dispersion can provide a useful approximation even in regions where it should not be applied and where there is no alternative continuum model for the spatial–temporal distribution of cells. To determine how well the model works, we compare results directly to individual-based simulations.

In addition to the applications specific to phytoplankton, results from this paper will be useful more generally for models of active suspensions and Taylor dispersion theory. Specifically, there has been extensive study as to the properties of dispersion due to the combination of micro-scale molecular diffusion and fluid advection, for example in the context of shear enhanced dispersion, chaotic advection and turbulence (e.g. Ottino 1990; Warhaft 2000; Ferreira de Sousa & Pereira 2009). In these studies, the starting point is an advection–diffusion equation in physical space for the passive scalar. The theory of generalized Taylor dispersion extends this to explore how diffusion in more general local variables can give diffusion at the macro-scale (Frankel & Brenner 1989). A key difference in the theory of generalized Taylor dispersion is that the starting point is a transport equation which includes diffusion in a micro-scale variable, for example in orientation space. This paper attempts to make progress in determining under what conditions this transport equation can be approximated by an advection–diffusion equation in physical space for the conserved scalar quantity.

We investigate how well population-level models describe the spatio-temporal distribution of gyrotactic phytoplankton for a selection of example flow fields. To simplify comparison between the individual-based simulations and population-level model, and in order to reduce the computational time required for the simulations, all motions are constrained to a two-dimensional vertical plane and the consequent population-level models are derived using an appropriate modification of the generalized Taylor dispersion theory. We note that care must be taken in extending the results to swimming particles free to move in three dimensions, as highlighted by Brenner (1979).

In § 2, we describe the two-dimensional, individual-level biased random walk and resulting population-level advection–diffusion model based on the generalized Taylor dispersion method (Hill & Bees 2002; Manela & Frankel 2003). Calculations are made to demonstrate how the mean-swimming direction and the diffusion tensor depend on the shear strength and type of flow. In § 3, we investigate dispersion in unidirectional flow fields. For this class of flows, the eigenvalues of the fluid velocity gradient tensor are all zero, that is the straining component of the flow cannot dominate the flow profile. In Couette flow, the shear is homogeneous and so the generalized Taylor dispersion theory is expected to hold. Furthermore, we can obtain simple analytic expressions for the equilibrium distribution of cells, providing validation of both the advection–diffusion-based and the individual-based simulations. For simple horizontal Couette flow, we demonstrate how using the calculated expressions for mean-swimming and diffusion, as opposed to simpler *ad-hoc* approximations, can alter the spatial distribution of the cells. For example, in the limit of strong shear, we obtain a shear-independent analytic asymptotic expression for the non-uniform equilibrium concentration. This is validated against individual-based simulations and is in contrast to previous predictions of a uniform concentration at equilibrium in the limit of strong shear. Furthermore, in simple horizontal Couette flow with zero or weak shear, discrepancies between the equilibrium distribution obtained from individual-based simulations and solutions to the population-level model highlight a failure of the population-level model to accurately represent reflective boundary conditions. For unidirectional flows with variable shear, such as Poiseuille flow, the mean-swimming direction and diffusion tensor vary in the cross-stream direction. For these flow fields, we are thus able to examine whether the population-level model based on the local shear is valid for non-homogeneous shear flows in situations where cells can swim between regions of differing shear. We explore the influence of the newly computed diffusion tensor on the phenomenon of gyrotactic focusing (Kessler 1985) for both spherical and non-spherical cells, and on the formation of phytoplankton thin layers (Durham *et al.* 2009). In § 4, we consider dispersion in a two-dimensional model vortex flow. In this case, there are regions where eigenvalues of the fluid velocity gradient have non-zero real part, that is regions of straining-dominated flow. In these regions, generalized Taylor dispersion may fail because of exponential divergence of particle positions. Furthermore, cells can be rapidly advected between regions of differing strain which, for non-spherical cells, is a significant deviation from the assumption that cells experience homogeneous shear. In order to examine this, transient and equilibrium numerical solutions of the advection–diffusion equation are compared with individual-based simulations in the two-dimensional box. Finally, in § 5, we make some concluding comments.

## 2. The model

We restrict attention to the two-dimensional plane denoted by unit vectors $(\boldsymbol{i}, \boldsymbol{j})$. We define the fluid velocity, $\boldsymbol{V}(\boldsymbol{x})$, and fluid velocity gradient, $\boldsymbol{G} = (\nabla \boldsymbol{V})^{\mathrm{T}}$, so that for homogeneous shear flow, we have $\boldsymbol{V}(\boldsymbol{x}) = \boldsymbol{V}(\boldsymbol{0}) + \boldsymbol{x} \cdot \boldsymbol{G}$. The in-plane vorticity is $\omega = G_{12} - G_{21}$ and the rate of strain tensor is $\boldsymbol{E} = \frac{1}{2}(\nabla \boldsymbol{V} + (\nabla \boldsymbol{V})^{\mathrm{T}})$.

### 2.1. *Individual-based model*

We consider a cell with swimming velocity $v_s \boldsymbol{p} = v_s(\sin\theta \boldsymbol{i} + \cos\theta \boldsymbol{j})$ that is also advected at the local fluid velocity, $\boldsymbol{V}(\boldsymbol{x})$. The swimming speed $v_s$ is assumed to be constant, but the direction is modelled by a biased random walk. At each small time

step, $\delta t$, the cell orientation to the vertical, $\theta$, is altered by an amount, $\delta\theta$, where $\delta\theta$ is a random variable taken from a normal distribution with mean $\mu$ and variance $\sigma^2$ given by

$$\mu = \left(-\frac{1}{2}\omega + \alpha_0(\sin(2\theta)E_{11} + \cos(2\theta)E_{12}) - \frac{1}{2B}\sin\theta\right)\delta t, \tag{2.1}$$

$$\sigma^2 = 2d_r\delta t, \tag{2.2}$$

where $d_r$ can be interpreted as a rotary diffusion coefficient; $E_{11}$ and $E_{12}$ are components of the rate of strain tensor; and, as before, $B$ a time scale for the cell to reorient towards the vertical ($\boldsymbol{j}$). The mean component of the motion models gyrotaxis and can be derived from (1.1) by setting $\boldsymbol{F} = \boldsymbol{j}$.

### 2.2. *Advection–diffusion model*

Following Hill & Häder (1997) and Manela & Frankel (2003), in the limit of $\delta t \to 0$, the random walk in orientation yields the following micro-scale model for $P(\boldsymbol{p}, \boldsymbol{x}, t)$, the probability of finding a cell with orientation $\boldsymbol{p}$ at position $\boldsymbol{x}$ at time $t$:

$$\frac{\partial P}{\partial t} + \nabla_{\boldsymbol{x}} \cdot ((\boldsymbol{V} + v_s\boldsymbol{p})P) + d_r\mathscr{L}P = 0, \tag{2.3}$$

where the linear operator $\mathscr{L}$ is defined as

$$\mathscr{L}f = -\frac{\partial}{\partial\theta}\left(\left(Pr\left(\frac{1}{2}\hat{\omega} - \alpha_0(\sin(2\theta)\hat{E}_{11} + \cos(2\theta)\hat{E}_{12})\right) + \kappa\sin\theta\right)f + \frac{\partial f}{\partial\theta}\right). \tag{2.4}$$

In the absence of the terms multiplied by $Pr$ and $\kappa$, the linear operator represents unbiased diffusion in orientation space. The term multiplied by $Pr$ represents a bias induced by the fluid shear; and $Pr$ is a non-dimensional measure of the shear

$$Pr = \frac{G}{d_r}, \quad \text{where} \quad \mathbf{G} = G\hat{\mathbf{G}}. \tag{2.5}$$

Here, $\hat{\omega}$ is the vorticity non-dimensionalized on $G$, and $\hat{E}_{11}$, $\hat{E}_{12}$ are components of the rate of strain tensor, also non-dimensionalized on $G$. The dimensional measure for the magnitude of the fluid velocity gradient, $G$, is chosen so that $\hat{\mathbf{G}}$ is $O(1)$, but the exact definition will depend on the particular flow field. The second term represents the bias due to gravitaxis and its relative importance is given by the non-dimensional parameter $\kappa$,

$$\kappa = \frac{1}{2d_r B}. \tag{2.6}$$

Modifying for two dimensions the previous three-dimensional results (Hill & Bees 2002; Manela & Frankel 2003), applicable for homogeneous shear flow subject to the constraint that the eigenvalues of $\mathbf{G}$ have zero real part, we find that on time scales long compared to $1/d_r$, the cell concentration, $n(\boldsymbol{x}, t)$ satisfies an advection–diffusion equation:

$$\frac{\partial n}{\partial t} = -\nabla\cdot\left((\boldsymbol{V} + v_s\overline{\boldsymbol{p}})n - \frac{v_s^2}{d_r}\boldsymbol{D}\cdot\nabla n\right), \tag{2.7}$$

where the mean-swimming direction, $\overline{\boldsymbol{p}}$, is given by

$$\overline{\boldsymbol{p}} = \int_0^{2\pi} \boldsymbol{p}f\,\mathrm{d}\theta, \tag{2.8}$$

and the non-dimensional diffusion tensor is given by

$$\boldsymbol{D} = \int_0^{2\pi} \left[ \boldsymbol{b}\boldsymbol{p} + \frac{Pr}{f} \boldsymbol{b}\boldsymbol{b} \cdot \hat{\boldsymbol{G}} \right]^{sym} \mathrm{d}\theta. \tag{2.9}$$

Here, $[\,]^{sym}$ denotes the symmetric part of the tensor.

The equilibrium orientation, $f(\theta)$, and vector $\boldsymbol{b}(\theta)$ satisfy

$$\mathscr{L} f = 0, \tag{2.10}$$

$$\mathscr{L} \boldsymbol{b} - Pr \boldsymbol{b} \cdot \hat{\boldsymbol{G}} = f(\theta)(\boldsymbol{p} - \overline{\boldsymbol{p}}), \tag{2.11}$$

subject to the integral constraints

$$\int_0^{2\pi} f \,\mathrm{d}\theta = 1, \quad \int_0^{2\pi} \boldsymbol{b} \,\mathrm{d}\theta = 0. \tag{2.12}$$

A simplified summary of the derivation of this result based on work by Frankel & Brenner (1991, 1993) is provided as online supplementary material, available at journals.cambridge.org/flm. The solution of this system confined to two dimensions is discussed in the Appendix. In particular, a numerical Galerkin method for arbitrary values of $Pr$ is derived which modifies previous methods used for three dimensions (Hill & Bees 2002; Manela & Frankel 2003) to two dimensions. New asymptotic limits for motions confined to two dimensions for weak and strong flow are also calculated explicitly.

2.2.1. *Properties of diffusion tensor for spherical cells in the absence of gravitactic bias*

As shown in the Appendix, § A.1, in the absence of flow, the diffusion tensor is similar to that proposed by Pedley & Kessler (1990), $v_s^2 \tau \,\mathrm{var}(\boldsymbol{p})$, provided the correlation time, $\tau$, is a correctly chosen function of the gravitactic bias, $\kappa$.

We now consider how the diffusion is altered by the flow in the special case of spherical cells in the absence of gravitactic bias, that is $\kappa = 0, \alpha_0 = 0$. With a suitable choice of axes, the most general homogeneous flow has velocity gradient

$$\hat{\boldsymbol{G}} = \begin{pmatrix} 0 & \alpha \\ 1 & 0 \end{pmatrix}. \tag{2.13}$$

Note that $\alpha = -1$ corresponds to pure rotation; $\alpha = 0$, simple shear flow; and $\alpha = 1$, pure straining motion. The theory of generalized Taylor dispersion is only valid if the eigenvalues of $\hat{\boldsymbol{G}}$ have zero real part, that is $\alpha \leqslant 0$, which corresponds to the cases where either the streamlines are closed $\alpha < 0$, or the flow is simple shear. When $\alpha > 0$, advection by the fluid motion alone leads to exponentially rapid divergence of the position vector of adjacent material points, and the theory fails (Frankel & Brenner 1991).

In this case, explicit expressions can be obtained from the diffusion tensor, as given in the Appendix, § A.4.1. From these calculations, we note that for pure rotation, the diffusion tensor is isotropic and independent of the vorticity. This can be expected as the flow field corresponds to solid-body rotation, and so, as we are neglecting inertial effects, we do not expect this flow field to modify the diffusion.

As depicted in figure 1, as straining motion is introduced, the diffusion tensor is modified for moderate values of the vorticity; specifically, diffusion is enhanced in the direction of the streamlines, $D_{xx}$, and reduced in the cross-stream direction, $D_{yy}$. Care should be taken when making a comparison with the classical Taylor dispersion phenomenon in which dispersion in the streamline direction is enhanced. In the

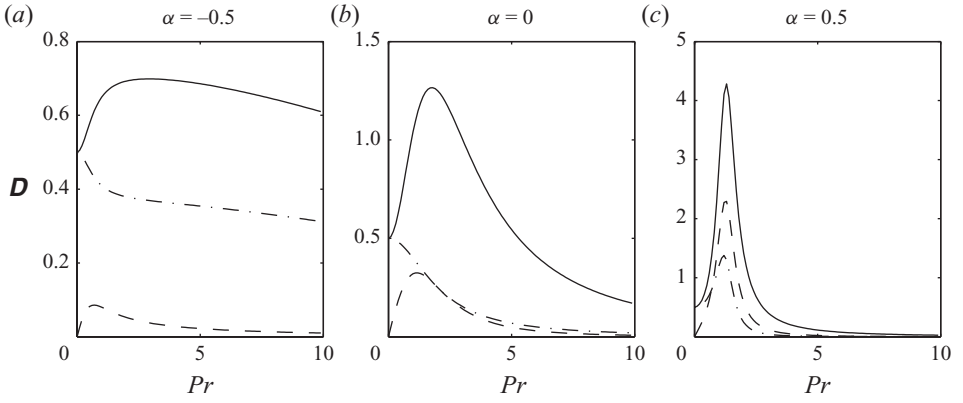


FIGURE 1. (*a–c*) Components of diffusion tensor as a function of non-dimensional shear, $Pr$, in the case of no gravitactic bias, $\kappa = 0$, and spherical cells, $\alpha_0 = 1$, for increasing values of strain, $\alpha = -0.5, 0, 0.5$: solid line $D_{xx}$; dash-dot $D_{yy}$; dash $D_{xy}$.

classical Taylor dispersion phenomenon, the effective diffusion tensor in physical space is unaltered by the flow, and it is the combination of cross-stream diffusion and shear that gives rise to the enhanced diffusion in the streamline direction. However, here we have found that shear modifies the physical space diffusion tensor in such a way that the classical Taylor dispersion mechanism may actually be reduced because of a reduction in the cross-stream diffusion, $D_{yy}$.

Although the generalized Taylor dispersion theory is not valid for $\alpha > 0$, we also plot the components of the diffusion tensor for $\alpha = 0.5$. Despite the theory not being valid, in the absence of any alternative population-level model, we shall compute the diffusion tensor for cells that experience a straining-dominated flow locally and investigate the resultant spatial distribution in § 4. Therefore, understanding the characteristics of the formal expression for the diffusion tensor given by (2.9), (2.11), and (2.12) is helpful to gain insight, for example, in understanding singular behaviour in the diffusion tensor (§ 4.3.2). For $\alpha = 0.5$, we see that there is a further enhancement in dispersion for moderate values of the vorticity due to the increased straining motion. For pure straining motion, $\alpha = 1$, the diffusivity tensor is singular when $Pr = 1$ as shown in the Appendix, § A.4.1.

For large $Pr$, except in the singular case of pure rotation, $\alpha = -1$, the diffusion tensor decays as $1/Pr^2$, according to the analytic expressions given in Appendix A.3. As previously noted (Hill & Bees 2002), this behaviour at large shear values is not captured by the diffusion tensor proposed by Pedley & Kessler (1990), $v_s^2 \tau \, \mathrm{var}(\boldsymbol{p})$, which tends to the identity matrix at large $Pr$ instead of vanishing.

### 2.3. *Numerical methods*

When solving the advection–diffusion equation numerically, it is convenient to non-dimensionalize lengths based on $L$, the size of the computational box, and non-dimensionalize time on a characteristic time scale for diffusion over the computational box. From (2.7), the diffusion tensor for the advection–diffusion model is $v_s^2/d_r$ multiplied by a non-dimensional tensor which is $O(1)$ in the absence of gravitactic bias or shear, and thus we take $L^2 d_r/v_s^2$ as a characteristic time scale for diffusion over a length $L$. This introduces two non-dimensional parameters into the problem:

the Péclet number which is given by

$$Pe = \frac{GL^2 d_r}{{v_s}^2}, \tag{2.14}$$

and $\epsilon$, a ratio of the typical correlation length scale of the random walk in the absence of bias to the length scale of the box:

$$\epsilon = \frac{v_s}{L d_r}. \tag{2.15}$$

We assume that $\epsilon$ is a small parameter, and take $\epsilon = 0.1$ in the numerical simulations. The non-dimensional shear, $Pr$, is given by

$$Pr = \frac{G}{d_r} = \epsilon^2 Pe. \tag{2.16}$$

2.3.1. *Finite-element method for advection–diffusion equation*

Equation (2.7) in non-dimensional form is given by

$$\frac{\partial n}{\partial t} = -\nabla \cdot \left( \left( Pe \hat{\boldsymbol{V}} + \frac{1}{\epsilon} \overline{\boldsymbol{p}} \right) n - \boldsymbol{D} \cdot \nabla n \right). \tag{2.17}$$

Noting that the mean-swimming direction, $\overline{\boldsymbol{p}}$, and diffusion tensor, $\boldsymbol{D}$, are functions of $\kappa$, $Pr$, and $\hat{\mathbf{G}}$, we see that the simulations will depend only on the local value of $\hat{\mathbf{G}}$ and the three parameters, $\kappa$, $Pe$ and $\epsilon$.

The governing advection–diffusion equation is solved using a Galerkin finite-element method. Equation (2.17) is transformed into a weak form on multiplication by a test function, $\psi(\boldsymbol{x})$, and by integration over the domain

$$\iint \left[ \frac{\partial n}{\partial t} + \nabla \cdot \left( \left( Pe \hat{\boldsymbol{V}} + \frac{1}{\epsilon} \bar{\boldsymbol{p}} \right) n - \boldsymbol{D} \cdot \nabla n \right) \right] \psi \, \mathrm{d}V = 0. \tag{2.18}$$

Integrating selected terms by parts and using the divergence theorem gives

$$\iint \left[ \left( \frac{\partial n}{\partial t} + Pe \, \hat{\boldsymbol{V}} \cdot \nabla n \right) \psi - \left( \frac{1}{\epsilon} n \bar{\boldsymbol{p}} - \boldsymbol{D} \cdot \nabla n \right) \cdot \nabla \psi \right] \mathrm{d}V + \oint \psi \left( \frac{1}{\epsilon} n \bar{\boldsymbol{p}} - \boldsymbol{D} \cdot \nabla n \right) \cdot \mathbf{d}\boldsymbol{S} = 0. \tag{2.19}$$

The second integral represents the normal flux out of the domain due to cell swimming and cell diffusion. In the majority of our computations, we impose no-flux boundary conditions, in which case the boundary integral is zero and the appropriate weak form is

$$\iint \left[ \left( \frac{\partial n}{\partial t} + Pe \, \hat{\boldsymbol{V}} \cdot \nabla n \right) \psi - \left( \frac{1}{\epsilon} n \bar{\boldsymbol{p}} - \boldsymbol{D} \cdot \nabla n \right) \cdot \nabla \psi \right] \mathrm{d}V = 0. \tag{2.20}$$

The cell concentration, $n$, is approximated using standard Lagrangian quadratic finite elements and the time derivative is approximated using an implicit second-order, backward difference scheme. The subsequent discrete linear system is assembled using the C++ library `oomph-lib` (Heil & Hazel 2006) and solved by a direct solver, SuperLU (Demmel *et al.* 1999). The mean cell swimming speed $\bar{\boldsymbol{p}}$ and diffusion tensor $\boldsymbol{D}$ are pre-computed using the Galerkin method described in the Appendix, § A.4. The estimated error in each element is calculated using Zienkiewicz & Zhu's (1992*a*, *b*) error estimator based on the recovery of concentration gradients. Elements

in which the estimated error exceeds a specified threshold, typically 0.1% of the global error norm, are refined by division into four equal elements. Continuity of the solution is enforced by constraining the values at any hanging nodes (see Demkowicz *et al.* 1989). For steady computations, the refinement is continued until the estimated error is below the threshold for every element, corresponding to an equidistribution of the error. For unsteady computations, one or two refinements were usually performed after each timestep.

For the unidirectional flow fields considered in § 3, the maximum number of elements is of the order $10^2$ in the direction over which the concentration varies. An exception to this is the early transient solutions in figure 3 which require a fine initial resolution to characterize cells initially concentrated at $y = 0$. For the two-dimensional periodic flow field depicted in figures 7 and 9, the maximum number of elements is of the order $10^4$. In unsteady simulations, a fixed time step of $\mathrm{d}t = 0.01$ is typically used, although a smaller time step of $\mathrm{d}t = 0.001$ is required to accurately capture early-time transient dynamics in figures 3(*d*) and 5(*e*). Simulations were validated by comparison with analytic solutions and individual-based simulations (see the following sections) and by repeating selected simulations with smaller error tolerances and timesteps.

2.3.2. *Individual-based modelling method*

Applying the above choice of non-dimensionalization to the individual-based model (IBM) described in § 2.1 in the limit of $\delta t$ tending to zero yields the following coupled ordinary-stochastic differential equation system for a single individual with position $\boldsymbol{x}_i$ and orientation $\theta_i$:

$$\begin{pmatrix} \dot{x}_i \\ \dot{y}_i \end{pmatrix} = Pe\hat{\boldsymbol{V}}(\boldsymbol{x}_i) + \frac{1}{\epsilon}\begin{pmatrix} \sin\theta_i \\ \cos\theta_i \end{pmatrix}, \tag{2.21}$$

$$\mathrm{d}\theta_i = \left(\xi Pe\left(-\frac{1}{2}\hat{\omega} + \alpha_0\sin(2\theta)\hat{E}_{11} + \alpha_0\cos(2\theta)\hat{E}_{12}\right) - \frac{\kappa}{\epsilon^2}\sin\theta\right)\mathrm{d}t + \sqrt{\frac{2}{\epsilon^2}}\,\mathrm{d}W, \tag{2.22}$$

where the $\theta_i$ equation is an expression for a biased correlated random walk with a bias given by the first (deterministic) term, and a variance given by the second term ($\mathrm{d}W$ is a standard Weiner process). In the full simulation, cells are gyrotactic and affected by vorticity which is modelled by setting $\xi = 1$. Simulations are also run for purely gravitactic cells by setting $\xi = 0$. The latter simulations are equivalent to a reduced population-level model in which the diffusion tensor and mean-swimming are computed assuming that the flow has no influence on behaviour ($Pr = 0$ in (2.4)).

Equations (2.21) and (2.22) are integrated at each time step following Sobczyk (1991): The position $(x_i^n, y_i^n)$ is updated to the new position $(x_i^{n+1}, y_i^{n+1})$ and $\theta_i^n$ is updated to $\theta_i^*$ via the fourth-order Runge–Kutta method for (2.21) and the deterministic part of (2.22) for a time step $\delta t$. A value $\delta\theta$ is drawn from the $N(0, 2/\epsilon^2\ \delta t)$ distribution and added to $\theta_i^*$ to give the new orientation $\theta_i^{n+1}$. For $Pe = 0, 1, 5$, the time step was taken as $\delta t = 10^{-3}$, and for $Pe = 10, 50$, the time step was reduced to $\delta t = 10^{-4}$. Convergence of results was checked by reducing the time step $\delta t$ by up to a factor of 10, and the convergence of equilibrium results was confirmed by extending the total duration of the simulation. Unless otherwise stated, the initial position and orientation of each cell was sampled from a uniform distribution.

To ensure conservation of cells, reflective boundary conditions corresponding to perfectly elastic collisions are imposed on both cell position and orientation at solid

boundaries. Specifically, when there are solid boundaries at $x=0$ and $x=1$, if the new $x$ lies outside this region, it is reflected in the relevant boundary back into the domain and $\theta$ is replaced by $-\theta$. Likewise, when there are solid boundaries at $y=0$ and $y=1$, then if the new $y$ lies outside this region, it is reflected in the relevant boundary back into the domain and $\theta$ is replaced by $\pi-\theta$.

For the unidirectional flows, the simulation was performed on a single PC with $10^5$ cells. For the two-dimensional flow field, the problem was split into 1000 separate runs with $10^5$ cells each and run on a Condor high-throughput computing system, where unused computing time on a network of PCs is used to perform large-scale computations.

## 3. Unidirectional flow

We consider unidirectional flow between two parallel walls in either the horizontal ($\boldsymbol{i}$) or vertical ($\boldsymbol{j}$) direction

$$\hat{\boldsymbol{V}} = V(y)\boldsymbol{i}, \quad y \in [0,1], \tag{3.1}$$

$$\text{or} \quad \hat{\boldsymbol{V}} = V(x)\boldsymbol{j}, \quad x \in [0,1]. \tag{3.2}$$

Note that the corresponding dimensional velocity is given by $GL\hat{\boldsymbol{V}}$, hence a suitable choice of $G$ for this geometry is $U/L$, where $U$ is a characteristic speed of the flow. We take no flux boundary condition on the walls, and seek one-dimensional solutions, $n(y,t)$ and $n(x,t)$ for the horizontal and vertical flows, respectively.

From (2.17), for horizontal flow, the steady equilibrium distribution satisfies

$$n(y) = n_0 \exp\left(\frac{1}{\epsilon}\int_0^y \nu_y \,\mathrm{d}y\right), \qquad \nu_y = \frac{\overline{p}_y}{D_{yy}}. \tag{3.3}$$

Locally, the flow field can be approximated by horizontal Couette flow with a shear strength that may vary with $y$. Whatever the shear, the vertical migration is always positive (see figure 2). Hence, for sufficiently small values of $\epsilon$, the cells form a thin layer near the top of the channel at equilibrium. Although the evolution towards equilibrium is affected by the shear distribution across the channel, the final state is well-approximated by the simple exponential

$$n = n_0 \,\mathrm{e}^{(1/\epsilon)\nu_y(1)y}, \tag{3.4}$$

where $\nu_y(1)$ is the value of $\overline{p}_y/D_{yy}$ calculated for the surface shear, $V'(1)$.

For vertical flow, the equilibrium solution for $n(x)$ is completely equivalent

$$n = n_0 \exp\left(\frac{1}{\epsilon}\int_0^x \nu_x \,\mathrm{d}x\right), \qquad \nu_x = \frac{\overline{p}_x}{D_{xx}}. \tag{3.5}$$

However, because $\overline{p}_x$, and hence, $\nu_x$, can be either positive or negative depending on the sign of the shear, the resulting distribution will depend on the shear profile $V'(x)$. This will be considered further in the context of gyrotactic focusing in § 3.2.

### 3.1. *Horizontal Couette flow*

For horizontal Couette flow, the shear is homogeneous, $V'(y)=1$, and so the diffusion tensor and mean-swimming direction are constant throughout the chamber. In this section, we focus attention on spherical cells, and will highlight a major discrepancy between the IBM and population-level model due to the reflective boundary conditions. In figure 2, the mean-swimming direction and components of diffusion tensor are plotted as functions of the shear strength, $Pr$, for an example

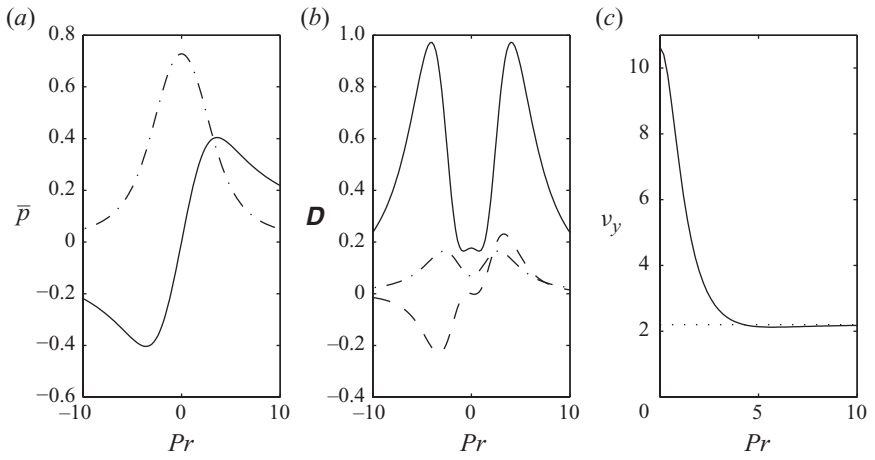


FIGURE 2. (*a*) Mean-swimming direction, $\bar{\boldsymbol{p}}$, (*b*) diffusion tensor, $\boldsymbol{D}$, and (*c*) ratio $\nu_y = \overline{p}_y / D_{yy}$ as a function of shear, $Pr$, for horizontal Couette flow with gravitactic bias $\kappa = 2.2$: solid line $\overline{p}_x$, $D_{xx}$; dash-dot $\overline{p}_y$, $D_{yy}$; dash $D_{xy}$. As $|Pr| \to \infty$, $\nu_y \to \kappa$, as indicated by dotted line.

value of gravitactic bias $\kappa$ of 2.2 (cf. Hill & Bees 2002). We see that there is a mean-swimming component in the direction of the flow, i.e. $\overline{p}_x$ is positive for positive values of $Pr$. This is because cells are more likely to be swimming upwards because of the bias, and the vorticity will, on average, rotate upward swimming cells to the right. The strong bias also modifies the diffusion tensor: for example, on comparing figure 2 with figure 1 ($\alpha = 0$), we see that the $D_{xx}$ component of the diffusion tensor peaks at a higher value of $Pr$ and has a lower maximum.

For horizontal Couette flow, the equilibrium distribution given by (3.3) is a simple exponential

$$n = n_0 \, \mathrm{e}^{(1/\epsilon)\nu_y y}. \tag{3.6}$$

The value of $\nu_y$ is plotted as a function of shear strength, $Pr$, in figure 2. For large values of $|Pr|$, asymptotic calculations (A 31) give the leading order expressions:

$$\overline{p}_y = \frac{2\kappa}{Pr^2}, \tag{3.7}$$

$$D_{yy} = \frac{2}{Pr^2}, \tag{3.8}$$

which give the leading order expression $\nu_y = \kappa$, and thus the equilibrium distribution becomes independent of the shear strength at large shear. Hence, although the ability to swim upwards is compromised because of the shear, there is a corresponding reduction in the diffusivity, which means that the equilibrium attained is an exponential distribution that depends only on the strength of the bias. Note, however, the time taken to reach this equilibrium will vary considerably because the diffusion rate scales as $1/Pr^2$ for large $Pr$. Also note that this asymptotic equilibrium distribution would not be predicted if using the diffusion tensor $v_s^2 \tau \, \mathrm{var}(\boldsymbol{p})$, which tends to the identity matrix at large $Pr$ instead of vanishing; in that case, the equilibrium distribution is uniform across the channel.

The equilibrium distribution is depicted in figure 3 as a function of shear, $Pr$. For a bias of $\kappa = 2.2$, with $\epsilon = 0.1$, the cells are confined to the top 5% of the channel at equilibrium. As the shear is increased, the concentration of cells near the upper wall

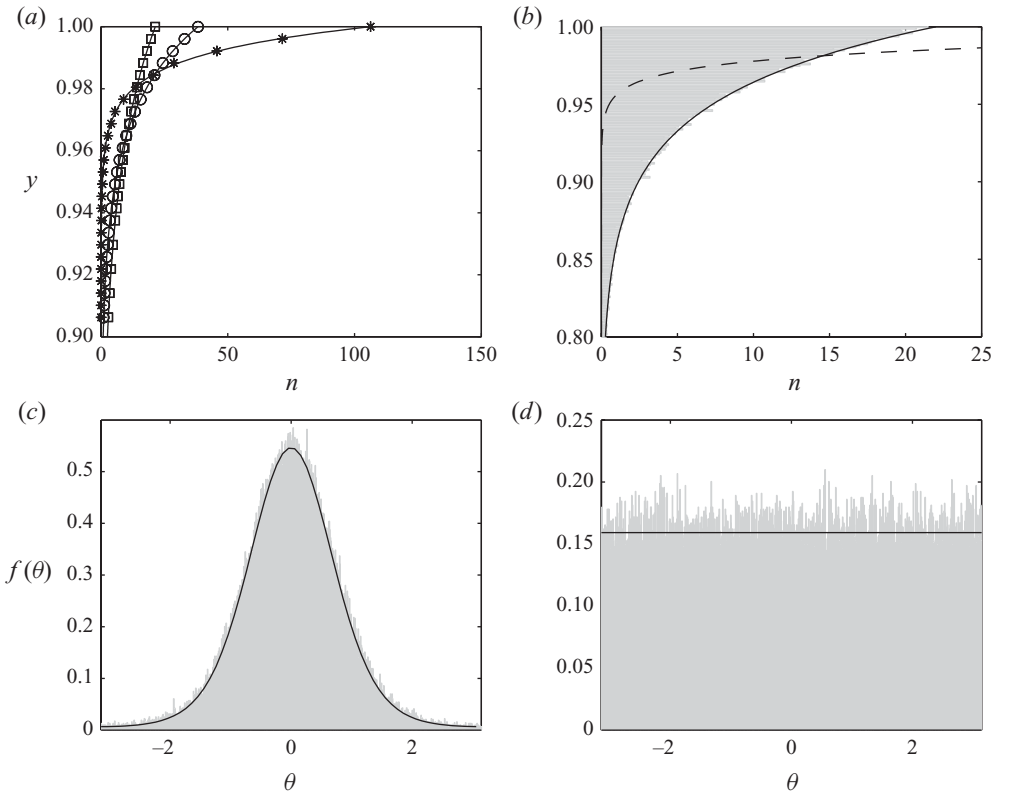


FIGURE 3. Distribution of cells in horizontal Couette flow with $\kappa = 2.2$. (*a*) Equilibrium distribution in the upper part of the channel for increasing values of shear $Pr$. Symbols are results from numerical solution of advection–diffusion equation: stars $Pr = 0$; circles $Pr = 2$; squares $Pr = 5$. Solid lines are analytic prediction, $n = n_0\, \mathrm{e}^{(1/\epsilon)v_y y}$. The asymptotic distribution for $Pr \to \infty$ is indistinguishable from $Pr = 5$. (*b*) The grey histogram is the equilibrium distribution from the IBM with $Pr = 0$. This agrees with the asymptotic distribution for $Pr \to \infty$ (solid line), but not the analytic prediction for $Pr = 0$ (dash line). (*c*) The orientation distribution at $t = 0.04$ with $Pr = 0$. The grey histogram represents results from the IBM, solid line is the distribution $f(\theta)$ as given in the Appendix, § A.1. (*d*) The uniform orientation distribution for $Pr = 0$ from the IBM obtained when cells have attained the equilibrium position distribution.

decreases and the cells spread across the channel, with the numerical solution showing excellent agreement with the analytic prediction. For shear $Pr = 5$, the concentration is indistinguishable from the asymptotic result of $n = n_0\, \mathrm{e}^{(\kappa/\epsilon)y}$.

Figure 3(*b*) depicts the equilibrium distribution found from the IBM in the no-flow case, $Pr = 0$. Interestingly, this distribution does not agree with the analytic prediction based on the advection–diffusion model at $Pr = 0$, but instead agrees with the analytic prediction for $Pr \to \infty$. Furthermore, the equilibrium distribution calculated using the IBM is identical for all values of $Pr$ tested. In other words, the equilibrium distribution appears to be independent of the flow. To understand this, it is necessary to consider in more detail how the cell orientation distribution is affected by the imposed boundary conditions.

In the absence of boundaries, the equilibrium orientation distribution found from the IBM in the no-flow case, $Pr = 0$, is the von Mises distribution, which is the equilibrium orientation distribution predicted from the population-level model

(see the Appendix, § A.1). This equilibrium orientation distribution can be seen at early times for the IBM with appropriate initial conditions (see figure 3*c*). Specifically, if cells are initially at $y = 0$, after a sufficient time for cells to randomly reorientate (a dimensional time of $1/d_r$, corresponding to a non-dimensional time of $\epsilon^2 = 0.01$), but not so long a time as to reach the top of the chamber and be reflected from the top boundary (a dimensional time of at least $L/v_s$, corresponding to a non-dimensional time of at least $\epsilon = 0.1$), the von Mises distribution is attained. In the derivation of the generalized Taylor dispersion theory, it is assumed that cell orientation is distributed according to this equilibrium distribution, and the population-level model is based on this assumption using (2.7)–(2.12). However, after reflecting off the boundaries many times and reorientating subsequent to reflection, the cells' equilibrium orientation distribution is indistinguishable from the uniform distribution (see figure 3*d*). This was confirmed using the IBM for $\kappa = 0.5$, 1 and 2.2, and moreover no spatial variation in the orientation distribution was found.

This discrepancy between the population-level model and IBM induced by the boundary conditions can be further explored if we consider the governing equation (2.3) describing the full random walk in the presence of flow. We find that $P(y, \theta)$, the equilibrium probability of finding a cell with orientation $\theta$ at vertical position $y$, satisfies the following equation:

$$\epsilon \frac{\partial}{\partial y}(\cos\theta P) - \frac{\partial}{\partial \theta}\left(\left(\frac{Pr}{2}\hat{\omega} + \kappa \sin\theta\right) P - \frac{\partial P}{\partial \theta}\right) = 0. \tag{3.9}$$

In addition, we require that the solution is periodic in $\theta$ and, because of the reflective boundaries, there can be no vertical flux of cells in the equilibrium distribution:

$$P(y, \theta + 2\pi) = P(y, \theta), \tag{3.10}$$

$$\int \cos\theta P \, \mathrm{d}\theta = 0. \tag{3.11}$$

Note that no assumptions regarding long-time approximations have been made in the derivation of this governing equation, and so the solution should be the exact equilibrium solution.

This system of equations has the following solution:

$$P(y, \theta) = \frac{1}{2\pi} n_0 \, \mathrm{e}^{(\kappa/\epsilon)y}, \tag{3.12}$$

which agrees with the results of the numerical simulations, in that it has the correct spatial distribution, $n(y) = \int P \, \mathrm{d}\theta = n_0 \, \mathrm{e}^{(\kappa/\epsilon)y}$ and the uniform orientation distribution. Furthermore, this solution agrees with the observation that the equilibrium distribution is independent of the flow in the IBM. As shown in figure 3(*b*), for the strong bias of $\kappa = 2.2$, this major difference in equilibrium orientation distribution due to the reflective boundary conditions can manifest itself in a significant difference in the predicted equilibrium spatial distribution in the no-flow case. For smaller values of $\kappa$ (for example, $\kappa = 0.5$, 1), the difference in equilibrium spatial distribution is less noticeable. As the shear increases, the equilibrium spatial distributions converge because the distribution found in the IBM is the same as that predicted from the advection–diffusion model in the asymptotic limit of large $Pr$.

This analysis demonstrates a failing of the generalized Taylor dispersion theory in the case where boundary conditions are critical in determining the spatial distribution. The fact that the IBM agrees with the solution of the underlying governing equation (2.3) demonstrates that it is more accurate than the solution of the advection–diffusion

equation, derived under the approximation that variation is occurring on long time and length scales compared to the scales associated with the random walk. We can gain insight into why the advection–diffusion model fails when $\kappa = O(1)$ by noting that the length scale of the equilibrium distribution is $O(\epsilon/\kappa)$ and so spatial variation occurs on a length scale comparable with the correlation length scale of the random walk, given by the non-dimensional parameter, $\epsilon$.

### 3.2. *Vertical Poiseuille flow*

For vertical Poiseuille flow, the eigenvalues of the fluid velocity gradient tensor are all zero, but cells can swim across streamlines and experience variable shear. In this section, the reflective boundary conditions do not have a strong influence on the equilibrium spatial distribution because the average swimming direction in the absence of flow is parallel, rather than normal, to the boundaries. Consequently, we find good agreement between the population-level model and IBM.

The approximate behaviour in vertical Poiseuille flow can be predicted by considering vertical Couette flow with $V'(x) = 1$. For small values of $|Pr|$, asymptotic calculation (A 5), (A 13) gives the following leading order expressions for the mean horizontal swimming velocity and $D_{xx}$ component of the diffusion tensor:

$$\overline{p}_x = \frac{Pr}{2\kappa}\left(\frac{1}{I_0(\kappa)^2} - 1 + \alpha_0\frac{I_2(\kappa)}{I_0(\kappa)}\right), \tag{3.13}$$

$$D_{xx} = \frac{1}{\kappa^2}\left(1 - \frac{1}{I_0(\kappa)^2}\right). \tag{3.14}$$

For large values of $|Pr|$, asymptotic calculations (A 33), (A 35) give the following leading order expressions for the mean horizontal swimming velocity and $D_{xx}$ component of the diffusion tensor:

$$\overline{p}_x = -\frac{\kappa}{Pr(1+\alpha_0)}, \tag{3.15}$$

$$D_{xx} = \frac{2-\alpha_0}{Pr^2(1-\alpha_0)(1+\alpha_0)^2}. \tag{3.16}$$

These asymptotic expressions were used when validating the numerical simulations. Note that for spherical cells, $\alpha_0 = 0$, both the asymptotic expressions for $v_x = \overline{p}_x/D_{xx}$ for large and small $Pr$ give $v_x \approx -\frac{1}{2}\kappa Pr$.

For vertical Poiseuille flow

$$\hat{\boldsymbol{V}} = x(1-x)\boldsymbol{j}, \tag{3.17}$$

we suppose that the mean-swimming and diffusivity can be computed based on the local shear. When the shear is positive, corresponding to anti-clockwise rotation of cells, the horizontal component of mean-swimming, $\overline{p}_x$, is negative corresponding to a tendency for cells to swim in the negative $x$-direction, and vice-versa for negative shear. This leads to the phenomenon of gyrotactic focusing in the centre of downwards pipe flow corresponding to negative values of $Pr$. The equilibrium distribution given by (3.5) is applied, where the expression for $v_x(y)$ is obtained based on the expressions for $\overline{p}_x$ and $D_{xx}$ for vertical Couette flow, but with $Pr$ replaced by the local shear strength in the Poiseuille flow, $Pr(1-2x)$. For example, an approximate analytic expression is found by using the asymptotic expressions for small $Pr$ (3.13), (3.14) to

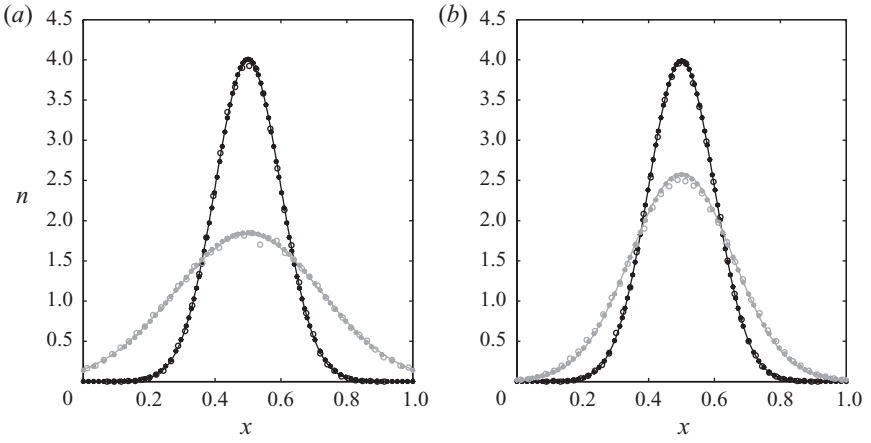


FIGURE 4. Equilibrium cell concentration in downward Poiseuille flow normalized so that the total cell population is unity. Solid line is the approximate Gaussian distribution given by (3.18); stars are numerical solutions of the advection–diffusion equation; circles are from the IBM. (*a*) Spherical cells, $\alpha_0 = 0$, with bias $\kappa = 1$ for increasing shear: grey line and symbols, $Pe = -200$; black line and symbols, $Pe = -1000$. (*b*) $\kappa = 5$, $Pe = -200$: grey line and symbols, non-spherical cells, $\alpha_0 = 0.9$; black line and symbols, spherical cells $\alpha_0 = 0$.

give the equilibrium distribution

$$n = n_0 \exp\left(\frac{-\epsilon\kappa Pe}{2} x(1-x)\left(1 - \alpha_0 \frac{I_2(\kappa)I_0(\kappa)}{(I_0(\kappa))^2 - 1}\right)\right), \tag{3.18}$$

where we have used (2.16) to write $Pr = \epsilon^2 Pe$ in order to give a more physically intuitive description in terms of the Péclet number, $Pe$. From this expression for the distribution, as depicted in figure 4, we see how increasing either the gyrotactic bias, $\kappa$, or the Péclet number increases the strength of the focusing, while increasing $\alpha_0$, i.e. considering more elongated cells, flattens the distribution. Again, note this asymptotic equilibrium distribution is not predicted using the diffusion tensor $v_s^2 \tau \, \mathrm{var}(\boldsymbol{p})$; in that case, once again, a uniform distribution is predicted at equilibrium for sufficiently strong flows, i.e. large $Pe$.

### 3.3. *Formation of phytoplankton thin layers*

As an example solution that displays interesting transient dynamics, we consider the following flow field which displays strong shear in a thin region of width $\delta$ around $y = 0.5$:

$$\hat{\boldsymbol{V}} = \tanh\left(\frac{y - 0.5}{\delta}\right)\boldsymbol{i}, \quad y \in [0, 1]. \tag{3.19}$$

This flow field was considered by Durham *et al.* (2009) who combined experiments and simple models to investigate whether gyrotaxis can lead to the formation of thin layers of phytoplankton. We note that the flow field does not satisfy the Navier–Stokes equations (except under the addition of artificial body forces), yet does provides a simple model of the physical system being studied. For this flow field, the horizontal component of the fluid velocity, mean-upswimming velocity and $D_{yy}$ component of the diffusion tensor based on the local shear are plotted in figure 5. In the region when there is a rapid change in fluid velocity, there is a big drop in upswimming and vertical diffusion. Also plotted in figure 5 are the transient solutions to the

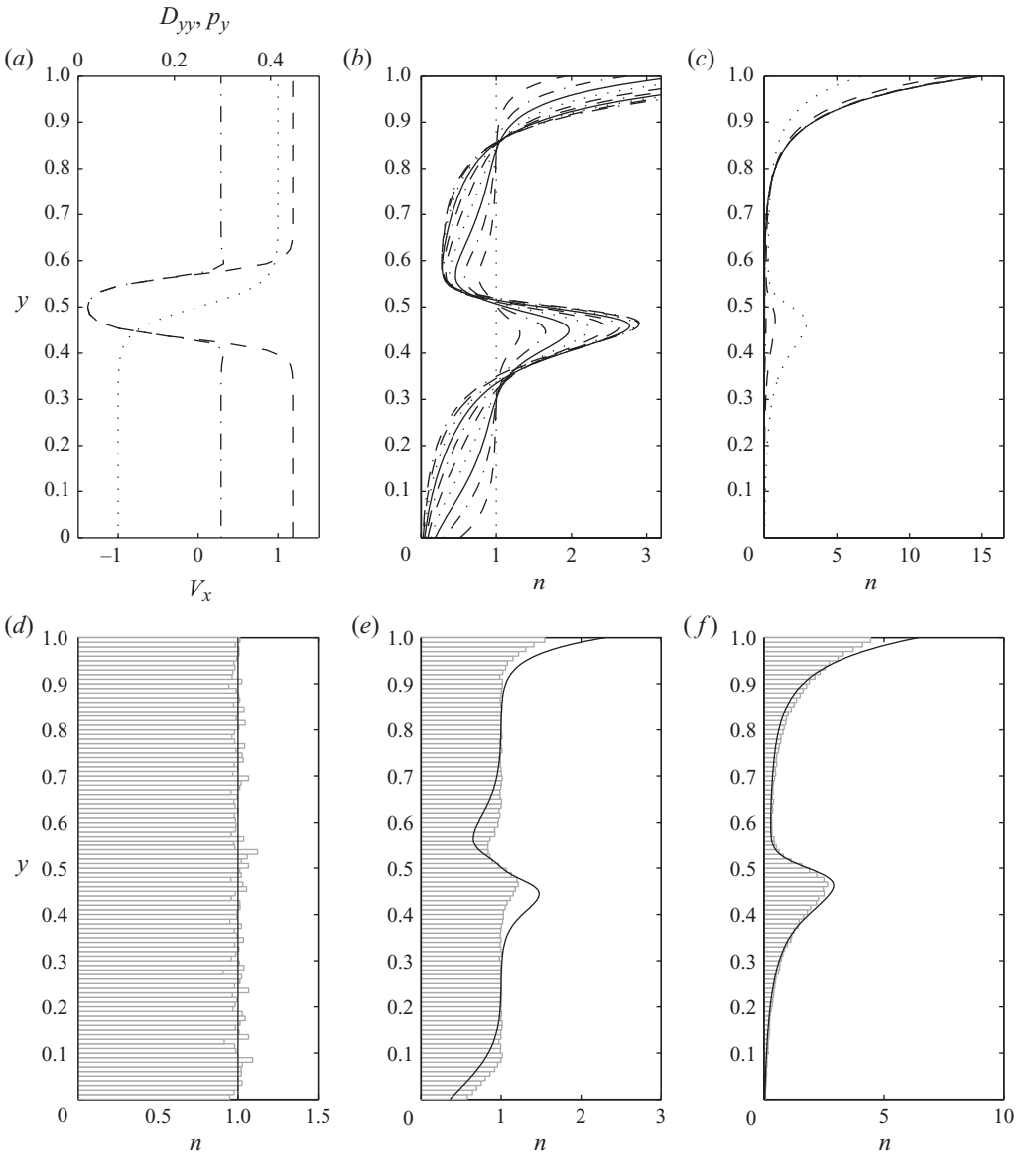


FIGURE 5. Formation of thin layer with parameter values $\delta = 0.05$, $\kappa = 1$, $Pe = 50$. (*a*) Horizontal fluid velocity, $V_x$ (dot line); mean vertical swimming direction $\overline{p_y}$ (dash line) and $D_{yy}$ component of the diffusion tensor (dash-dot line). (*b*) Numerical transient solution of advection–diffusion equation: lines plotted at intervals of $\mathrm{d}t = 0.01$ for $t = 0$ (uniform distribution) to $t = 0.1$. (*c*) Dotted line, solution for $t = 0.1$; dash line, solution for $t = 0.5$; solid line, still fluid equilibrium solution $n = n_0\, \mathrm{e}^{(1/\epsilon)v_y y}$, with $v_y$ calculated for the zero flow case $Pe = 0$. The solution of the advection–diffusion equation for $t \geqslant 1$ is indistinguishable from the still fluid equilibrium solution. (*d*)–(*f*) Comparison of results from IBM (histogram) with numerical solution of advection–diffusion equation (solid line) at (*d*) $t = 0$, (*e*) $t = 0.01$ and (*f*) $t = 0.1$.

advection–diffusion equation. Starting from an initially uniform distribution, cells form a thin layer due to the suppression of upswimming in the strong shear layer. Although the diffusivity and upswimming are small in this region, they are not zero, and eventually cells pass through this region and ultimately form a layer of cells at

the top of the channel. As discussed previously, the equilibrium distribution can be approximated by a simple exponential $n = n_0 \mathrm{e}^{(1/\epsilon)v_y y}$, where $v_y$ is the value of $\overline{p}_y/D_{yy}$ in the region containing the bulk of the cells. In this flow field, there is zero shear in the top layer, and so the equilibrium solution is indistinguishable from the still fluid case, as shown in figure 5.

A comparison of the IBM with the solution of the advection–diffusion equation at early times is shown in figure 5(*d–f*). In the region of rapidly changing shear, we note a slight discrepancy between the IBM and the solution of the advection–diffusion equation in figure 5(*e*). As described in § 2.3, the numerical schemes were particularly sensitive to the choice of time step for these early transient distributions. In particular, we verified that the distribution shown in figure 5(*e*) was fully converged by comparing the solution of the advection–diffusion equation taking $\delta t = 10^{-3}$ and taking $\delta t = 10^{-4}$. For the IBM, comparison of the solution with $\delta t = 10^{-4}$ and $\delta t = 10^{-5}$ demonstrated convergence.

The difference between the solution of the advection–diffusion equation and IBM could be because cells experience rapidly changing shear when crossing the thin layer, whereas the theory of generalized Taylor dispersion only applies to homogeneous shear. Specifically, cells with a strong bias towards swimming upwards can swim across the layer and experience rapidly changing shear on a non-dimensional time scale $O(\epsilon\delta) = 0.005$ which is faster than the non-dimensional correlation time of the random walk, $\epsilon^2 = 0.01$. Nonetheless, the agreement in the layer is excellent by $t = 0.1$. However, we note that the distribution near the upper boundary is more diffuse for the IBM than the corresponding solution of the advection–diffusion equation, which is likely because of the influence of boundary effects as previously discussed for Couette flow.

### 3.4. *Conclusions*

In unidirectional flows, the results of the individual and population models are generally in good agreement because cells can only move between regions of varying shear by swimming, which occurs on relatively long time scales; and so the theory of generalized Taylor dispersion is expected to hold. Both models successfully predict the phenomena of gravitactic focusing and shear-induced formation of thin layers.

Nonetheless, discrepancies between the models do arise due to (i) the boundary conditions imposed on the individual model, which can dominate the equilibrium orientation distribution, as found for horizontal Couette flow; and (ii) phenomena that occur on spatial and temporal scales that are too short for the population model to apply, such as the early-time dynamics of the shear-induced formation of thin layers.

## 4. Two-dimensional flow

We now consider two-dimensional flow in a box $x \in [0, 1]$, $y \in [0, 1]$ with a fluid velocity $\hat{\boldsymbol{V}}$ that represents a convection cell

$$\hat{\boldsymbol{V}} = \pi(\sin(\pi x)\cos(\pi y), -\cos(\pi x)\sin(\pi y))^{\mathrm{T}}. \tag{4.1}$$

Once again, we note that this flow field does not satisfy the Navier–Stokes equations (except under the addition of artificial body forces), yet does provide a simple model of the mixing behaviour present in a convection cell. In this flow field, the shear is not homogeneous and, moreover, the real parts of the eigenvalues of the velocity-gradient tensor, $\hat{\mathbf{G}}$, are non-zero in the straining-dominated corner regions; i.e. outside the

square with vertices $\{(1/2, 0), (1/2, 1), (0, 1/2), (1, 1/2)\}$. Although generalized Taylor dispersion theory is not expected to apply in these regions, we shall continue to use it to compute the macroscopic advection and diffusion coefficients based on local values of shear.

For this flow field vorticity contours align with the streamlines and so spherical cells will only experience variation in viscous torque when they swim across streamlines. In § 3.2, variation in shear due to swimming across streamlines was shown not to invalidate the generalized Taylor dispersion theory, and so we do not expect this source of variation to be significant here. However, non-spherical cells will be advected between regions where they experience different viscous torques because the rate of strain varies along streamlines. At sufficiently high fluid velocities, this advection between regions of differing strain can cause a major failing in the generalized Taylor dispersion theory, as will be demonstrated in § 4.1 when we consider the spatial distribution in the absence of gravitactic bias.

Restricting attention to spherical cells, we then examine in more detail the failings associated with using generalized Taylor dispersion theory based on local values of shear in straining-dominated regions. Specifically, we solve the advection–diffusion equation with no-flux boundary conditions on the walls $x = 0, 1$, $y = 0, 1$ and compare the results with an individual-based simulation. The solution depends on three key parameters: $\kappa$ the strength of gravitactic bias; $Pe$, the strength of the advection and $\epsilon$, the ratio of the length scale of random walk to the convection cell size, which we take as 0.1 in the numerical simulations.

### 4.1. *No bias*

In the absence of gravitatic bias, Torney & Neufeld (2007) demonstrated that strongly elongated particles aggregated at the edges of convection cells. In contrast, we now demonstrate that applying the method of generalized Taylor dispersion theory based on the local shear predicts that cells are uniformly distributed. From (2.4), the local equilibrium orientation distribution satisfies

$$\frac{\mathrm{d}}{\mathrm{d}\theta}\left(Pr\left(\frac{1}{2}\hat{\omega} - \alpha_0(\sin(2\theta)\hat{E}_{11} + \cos(2\theta)\hat{E}_{12})\right) f + \frac{\mathrm{d}f}{\mathrm{d}\theta}\right) = 0. \tag{4.2}$$

By symmetry, the solution to this must satisfy $f(\theta) = f(\theta + \pi)$, and hence the mean-swimming direction, $\overline{\boldsymbol{p}}$, is zero. The advection–diffusion equation (2.17) for the cell concentration with zero mean-swimming and no flux boundary conditions has a uniform equilibrium solution. In contrast, in figure 6, we see that in the IBM strongly elongated particles do aggregate at the edges of the box, although the effect of rotational diffusion can significantly reduce the aggregation. Results of Torney & Neufeld (2007) demonstrate significant aggregation when the ratio of swimming speed to flow speed, which we here denote by $\mathscr{V}$, is 0.016 and state that these hold for $d_r \leqslant U_0/L$, where $U_0$ corresponds to $\pi GL$ in our description of the flow field. In our simulations, where lengths are non-dimensionalized on $L$ and time on the time scale for diffusion over this length, $L^2 d_r / v_s^2$, we have a non-dimensional swimming speed of $1/\epsilon$ and non-dimensional flow speed $\pi Pe$. Thus, we obtain the ratio of speeds, $\mathscr{V} = 1/(\epsilon Pe\pi)$, which we take to be 0.016. The restriction on the rotational diffusion, $d_r \leqslant U_0/L$, corresponds to $\epsilon^2 Pe\pi \geqslant 1$ and for the simulation presented in figure 6 which includes rotational diffusion we take $\epsilon^2 Pe\pi = 2$. This choice of parameters corresponds to taking $Pe = 620$ and $\epsilon = 0.032$. For the deterministic individual-based simulations, the same values of $Pe$ and $\epsilon$ were used but the stochastic component of the model given by (2.21) and (2.22) was eliminated.

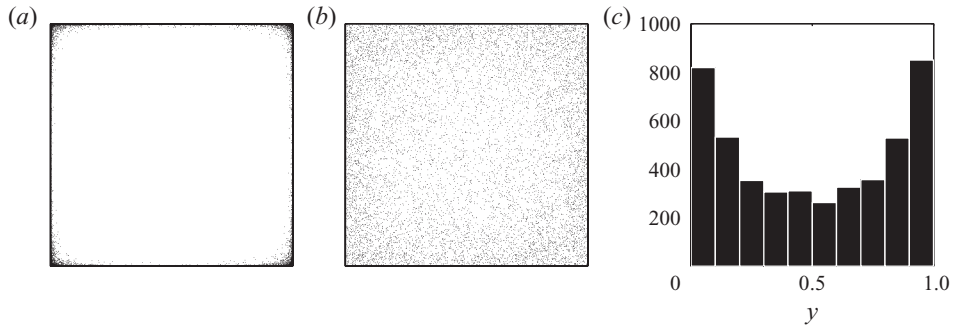


FIGURE 6. IBM equilibrium results for non-spherical cells, $\alpha_0 = 1$: ($a$) cell positions for deterministic simulations; ($b$) cell positions for simulations which include rotational diffusion; ($c$) histogram of vertical position for cells with horizontal position $x \in (0.2, 0.8)$ for simulation with rotational diffusion. Parameters chosen to compare with figure 1 of Torney & Neufeld (2007) correspond to $Pe = 620, \epsilon = 0.032$, see main text.

### 4.2. *Weak flow*

In the absence of flow, $Pe = 0$, the equilibrium solution is the simple exponential distribution, i.e. $n = n_0 \exp(\nu y)$, where we have defined $\nu = 1/(\epsilon v_y) = \overline{p}_y/(\epsilon D_{yy})$. An example plot of this is given in figure 3($a$) with $Pr = \epsilon^2 Pe = 0$.

Flow will modify this exponential distribution through two mechanisms: (i) advection by the flow; (ii) modification of the mean-swimming and diffusion coefficients. The quantity $Pr = \epsilon^2 Pe$ determines how significantly the mean-swimming and diffusion coefficients are modified and so, as we typically take $\epsilon \ll 1$, and for weak flow, $Pe \ll 1$, only the first mechanism is likely to be important. We can therefore approximate the case of weak flow by considering purely gravitactic cells, that is cells whose mean-swimming and self-diffusion is not modified by the flow. For such cells, the mean-swimming direction is directly upwards, and we can rewrite the non-dimensional governing equation as

$$\frac{\partial n}{\partial t} = -\nabla \cdot \left( \left( Pe\boldsymbol{V} + \frac{1}{\epsilon}\overline{p}_y \boldsymbol{j} \right) n - \boldsymbol{D} \cdot \nabla n \right), \tag{4.3}$$

where $\overline{p}_y$ and $\boldsymbol{D}$ are values of the mean-swimming and self-diffusion calculated when flow has no influence on behaviour. For weak flow, $Pe \ll 1$, an analytic expression for the leading order correction to the still-fluid exponential distribution for the convection cell flow field can be found and was used for code validation. (Details in online supplementary material).

### 4.3. *Spherical cells in moderate and strong flow*

#### 4.3.1. *Numerical solution of advection–diffusion equation*

Example equilibrium solutions for spherical cells for increasing values of $Pe$ are given in figure 7. For small values of $Pe$, the flow advects the thin upper layer of cells towards the top-left corner. As $Pe$ is increased, cells are entrained into the main bulk of the convection cell. As $Pe$ is increased further, the cell concentration is approximately uniform except for boundary layers which form in the numerical solution of the advection–diffusion equation. For $Pe = 5$ and $Pe = 10$, the maximum value of the concentration in the top-left corner is smaller for the full solution than for the reduced solution, in which the diffusion tensor and mean-swimming are computed when the flow has no influence on behaviour ($Pr = 0$ in (2.4)) (see table 1). In contrast,

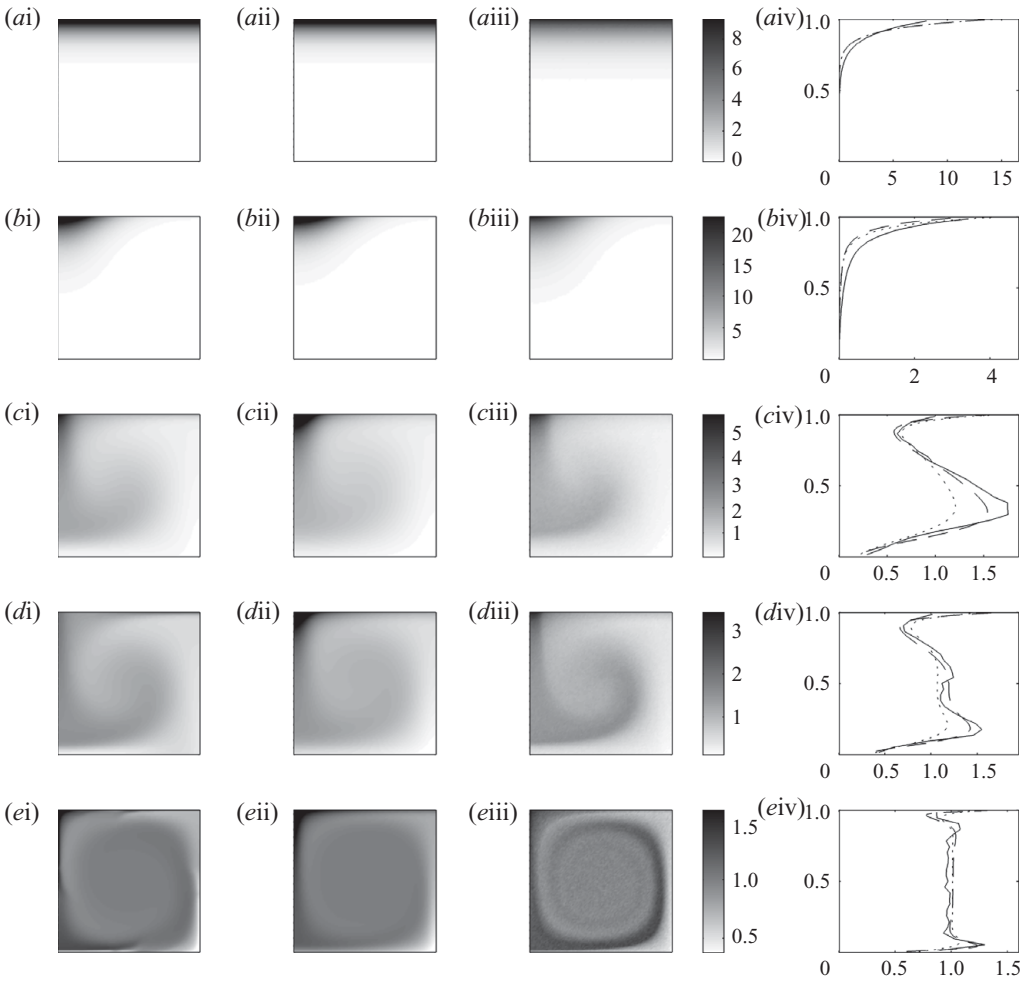


FIGURE 7. Equilibrium cell concentration for spherical cells, $\alpha_0 = 0$, with gravitactic bias $\kappa = 1$ for increasing values of $Pe$: (*a*) $Pe = 0$, (*b*) $Pe = 1$, (*c*) $Pe = 5$, (*d*) $Pe = 10$, (*e*) $Pe = 50$. (*a*i–*e*i) are the solutions of full advection–diffusion equation and (*a*ii–*e*ii) are solutions with mean-swimming and diffusion calculated for when flow has no influence on behaviour. (*a*iii–*c*iii) are solutions from the IBM. The grey scale is based on the minimum and maximum concentrations found in the IBM solution. (*a*iv)–(*e*iv) show the concentration at $x = 0.5$ as a function of $y$ for the IBM (solid line), full numerical solution of advection–diffusion equation (dash line) and solutions with mean-swimming and diffusion calculated for when flow has no influence on behaviour (dotted line).

for $Pe = 50$, the maximum value of the concentration in the top-left corner is larger for the full solution than for the reduced solution. Although the distribution shows the same general characteristics in the bulk of the region, the full solution does display sharper gradients in cell concentration than the reduced solution, as highlighted by the concentration slice at $x = 0.5$ at $Pe = 5$ and $Pe = 10$.

4.3.2. *Singularities in the diffusion in straining-dominated regions*

As previously discussed in § 2.2.1, the generalized Taylor dispersion theory is not valid in straining-dominated regions, yet, in the absence of any alternative population-level model, we have used the formal expression for the diffusion tensor obtained

| $Pe$ | Full solution | Reduced solution | IBM |
|---|---|---|---|
| 0 | 15.02 | 15.02 | 9.27 |
| 1 | 41.88 | 46.62 | 22.53 |
| 5 | 6.11 | 16.28 | 5.50 |
| 10 | 2.00 | 9.22 | 3.33 |
| 50 | 11.09 | 3.55 | 1.60 |

TABLE 1. Maximum concentration at top-left corner for increasing values of $Pe$ as computed using solution of full advection–diffusion equation, reduced solution with mean-swimming and diffusion calculated for when flow has no influence on behaviour, and IBM solution.

via the theory to model the spatial distribution in the convection cell. We now explore further the breakdown of this theory as evidenced by the differences in cell concentration between full and reduced simulations in the top-left corner by considering the pure-straining flow on the boundaries of the convection cell.

As discussed in § 2.2.1, for such pure straining flow given by

$$\hat{\mathbf{G}} = \begin{pmatrix} 0 & 1 \\ 1 & 0 \end{pmatrix}, \tag{4.4}$$

in the absence of bias the diffusion tensor becomes singular as the shear strength, $Pr = G/d_r = \epsilon^2 Pe$, approaches unity. We now consider where the singularity in the $D_{yy}$ component of the diffusion tensor occurs on the left boundary of the cell. Symmetry arguments give the relationship on the other boundary regions and for the $D_{xx}$ component of the diffusion tensor. On the left boundary, the eigenvalues of $\hat{\mathbf{G}}$ are $\pm\pi^2\cos(\pi y)$ and so when $\pi^2\epsilon^2 Pe < 1$, the diffusion tensor is nowhere singular, and $D_{yy}$ will take its maximum value at the top-left corner, and be a monotonically increasing function on the left boundary. As $\pi^2\epsilon^2 Pe$ approaches 1, $D_{yy}$ increases and tends to $\infty$ in the top-left corner. For $\pi^2\epsilon^2 Pe > 1$, the singularity moves downwards towards $y = 0.5$ as $\pi^2\epsilon^2 Pe \to \infty$. Although introducing bias, i.e. taking a non-zero value of $\kappa$, modifies exactly when the transition occurs, the qualitative argument still holds, as shown in figure 8: up to $Pe = 10$, the maximum value of $D_{yy}$ is at the top-left corner which increases for increasing values of $\epsilon^2 Pe$. This enhanced diffusion in the top-left corner is the primary reason why the cell concentration at the top-left corner in the full solution is lower than for the solution calculated for when flow has no influence on behaviour (see table 1). However, in contrast, for $Pe = 50$, the $y$ component of the diffusion in the top-left corner is lower than that of the reduced solution. Furthermore, this component has two singularities when $x = 0$, which results in non-smooth behaviour in the concentration profile near the boundaries, as shown in figure 7.

4.3.3. *Comparison with IBM*

As shown in figure 7, the individual-based simulation shows the same general pattern as the numerical solution of the advection–diffusion equation. As discussed in the context of unidirectional flow, in the absence of fluid advection, $Pe = 0$, the IBM has a broader equilibrium distribution in the $y$-direction because of boundary effects. For moderate flow strength, $Pe = 5$ and $Pe = 10$, the IBM is in better agreement with the full numerical solution than for the reduced solution. For example, the full solution better matches the sharp gradients in cell concentration than the reduced solution, as

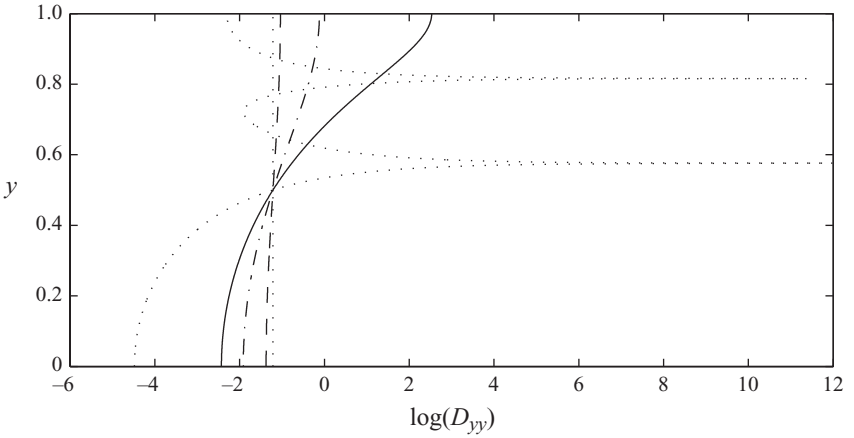


FIGURE 8. $D_{yy}$ component of diffusion tensor at $x = 0$ as a function of $y$ for increasing $Pe$: $Pe = 0$, dot; $Pe = 1$, dash; $Pe = 5$ , dash-dot; $Pe = 10$, solid; $Pe = 50$, dot. For $Pe \leqslant 10$, $D_{yy}$ is a monotonically increasing function of $y$. When $Pe = 50$, a bifurcation has occurred causing the diffusion singularity to split and to move away from $y = 1$.

highlighted by the concentration slice at $x = 0.5$. Also, the peak concentration near the top-left corner in the IBM better matches the full solution maxima than the reduced solution maxima (see table 1). For $Pe = 50$, in contrast to the numerical solution of the advection–diffusion equation, concentration peaks are not observed in the top-left corner which is likely to be because of the reflective boundary conditions, as found in the unidirectional simulations. The sharp gradients found in the IBM at $x = 0.5$ are better captured by the full solution, but the sharp gradients at larger values of $x$ were not well-captured in the advection–diffusion models. Discrepancies between IBM and the full solution are likely to be partly due to the unrealistic values of the diffusion tensor in the straining-dominated regions where the generalized Taylor dispersion method is not predicted to hold. Nonetheless, the agreement between the IBM and advection–diffusion equation remains reasonable in the lower left corner of the domain, which suggests that a localized breakdown of the generalized Taylor dispersion does not necessarily invalidate the results throughout the entire domain.

### 4.3.4. *Transient distribution*

An example transient concentration distribution computed using the population-level model is shown in figure 9. The initial condition is a normalized Gaussian of radius $1/\sqrt{50}$ centred at $x = 0.75$, $y = 0.5$. Interestingly, despite the large modification in the diffusion tensor in the corner regions, the overall spatial–temporal distribution is not dramatically altered from the prediction made using the diffusion values calculated for when flow has no influence on behaviour. A possible explanation for this is that in the bulk central area of the convection cell, the velocity field is approximately pure rotation, for which the method of generalized Taylor dispersion predicts no modification of the diffusion tensor in the absence of gravitactic bias for spherical particles. Also plotted in figure 9 is the IBM solution both including the effect of flow (gyrotaxis), and neglecting it. In the latter case, cells are advected by the flow but their swimming behaviour is unaltered by shear. Interestingly, the effect of including gyrotaxis is very different with the IBM compared to the numerical solution of the advection–diffusion equation. This is perhaps because the population-level model is

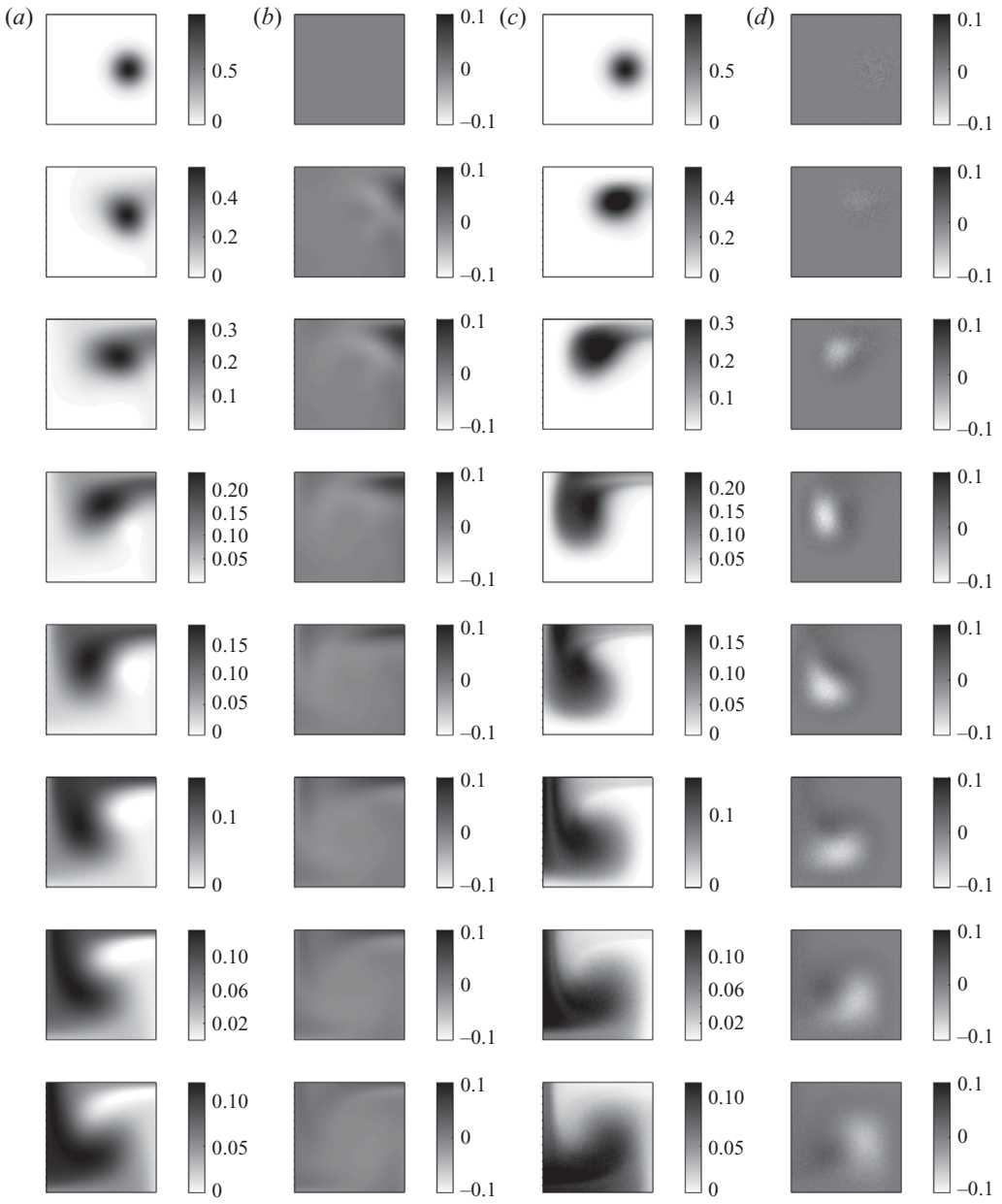


FIGURE 9. Cell concentration for parameter values $\alpha_0 = 0$, $\kappa = 0$, $Pe = 10$: (*a*) solution of full advection–diffusion equation at increments of $\mathrm{d}t = 0.01$ from $t = 0$ to $t = 0.08$; (*b*) full solution minus reduced solution; (*c*) solution of gyrotactic IBM at same times; (*d*) gyrotactic IBM solution minus reduced IBM solution.

not appropriate at short time scales, as found in the unidirectional studies. At early times in the IBM, we see that gyrotaxis enhances the dispersion of the cells: decreasing the maximum concentration in the region of high-cell concentration and increasing the concentration at the periphery. At later times, we see a more complex behaviour.

## 5. Summary and concluding remarks

We have investigated the spatial distribution of gyrotactic swimming micro-organisms in a range of flow fields based on a population-level model derived via the method of generalized Taylor dispersion, and an individual-based stochastic simulation. Analytic solutions have been compared to numerical solutions, and limiting asymptotic results for large and small Péclet numbers have been derived. We have attempted to explain why the different methods sometimes showed good agreement and other times did not.

For gyrotactic focusing in pipe flow, the numerical methods agreed well with each other and with new asymptotic calculations for both spherical and non-spherical cells. Furthermore, the complex expression for the diffusion tensor derived using the generalized Taylor dispersion method was necessary to capture the horizontal spatial distribution observed in experiments. It would be of interest to investigate what the implications are for other phenomena, such as gyrotactic plume formation, and to determine the accuracy of previous calculations which assumed a constant cell swimming diffusivity and a deterministic orientation direction (e.g. Ghorai & Hill 1999). Recent work has examined how the active swimming behaviour of gyrotactic cells modifies the spatial dispersion in a pipe flow from the classical Taylor–Aris results (Bees & Croze 2010). This work used a less rigorous population-level model than presented here for the cell concentration which predicts a uniform horizontal distribution of cells at sufficiently high flow rates. Extending the analysis presented here to allow for swimming in three dimensions, in combination with the analysis of Bees & Croze (2010), will provide further insight into how actively swimming micro-organisms disperse in flow and has the potential to be experimentally testable. We also found good agreement between both methods in the example application to the formation of thin phytoplankton layers.

For horizontal Couette flow, we found the method of generalized Taylor dispersion could lead to spatial distributions which differed from the individual-based simulation because of boundary effects. Specifically, we found that, because of the no-flux boundary conditions on the top and bottom walls, the equilibrium orientation distribution was uniform in contrast to the von Mises distribution predicted in the absence of boundaries which forms the basis of the generalized Taylor dispersion method. When the bias in upswimming was strong, this resulted in a significant difference in the equilibrium spatial distribution between the IBM and the population-level model, and, in particular, we found that the equilibrium spatial distribution was independent of the shear strength.

For two-dimensional flow in a box, there were discrepancies between the IBM and the population-level model which were associated with application of the generalized Taylor dispersion method beyond its range of applicability. At sufficiently high values of the Péclet number, cells were rapidly advected between regions of differing strain which, for non-spherical cells, is a significant deviation from the assumption that cells experience homogeneous shear. As previously found by Torney & Neufeld (2007), this led to a significant aggregation of cells near the boundaries in the IBM even in the absence of gyrotactic bias whereas the population-level model had a uniform distribution at equilibrium. Discrepancies between the IBM and the population-level model were also observed near the boundaries of the convection cell for spherical cells subject to gyrotactic bias, for the same reasons as found for horizontal Couette flow. Furthermore, in straining-dominated regions, there were singularities in the diffusion tensor computed using the generalized Taylor dispersion method, which is

to be expected as the method is only valid if the real parts of the eigenvalues of $\hat{\mathbf{G}}$ are non-zero. However, in the presence of gravitactic bias, the full population-level model better matched the equilibrium solution obtained from the IBM than did the reduced population-level model where the diffusion tensor and mean-swimming were computed for when flow has no influence on behaviour. In particular, the full model was able to capture the sharp concentration gradients in the bulk of the convection cell at moderate flow strengths.

Several open questions remain as regards this paper. We have not closed the question of what happens if cells experience rapidly changing shear. In the work presented on horizontal flow with varying shear we showed how the method of generalized Taylor dispersion remains a good approximation in situations where cells can swim between regions of differing shear and thus experience non-homogeneous shear. However, in that case, the cells typically only experience slowly varying shear, as cells swim relatively slowly. In contrast, for two-dimensional flow in a box, we found significant deviations between the IBM and population-level model when we considered non-spherical cells which were rapidly advected between regions of differing strain. A natural extension is to examine a three-dimensional flow field where cells are advected between regions of varying shear, for example constant longitudinal advection within a cylindrical tube rotating at a spatially variable rate. This theoretical flow field could have the feature that the real part of the eigenvalues of the fluid velocity gradient is zero, thus allowing one to examine how well the population-level model describes the spatial distribution of phytoplankton which experience rapidly changing shear without the added complication of straining-dominated regions. We have also not closed the question of what population-level model should be used in straining-dominated regions. In the two-dimensional flow considered in this paper, boundary effects confounded comparison between the population-level model and the IBM. A numerical investigation using a theoretical flow field which has straining-dominated regions but with periodic boundaries could therefore be helpful to understand what happens in straining-dominated regions. In the preliminary part of work by Morris & Brady (1996), these authors highlight an alternative method for analysing self-diffusion in sheared suspensions. Specifically, they give an explicit expression for the spatial distribution of a solute diffusing in any linear shear flow through the use of spatial Fourier transforms. This approach may be useful to further investigate what happens in straining flow for the governing transport equation considered in this paper which includes diffusion in orientation space rather than starting with a diffusion model in physical space for the conserved scalar quantity.

In order to focus attention on how well population-level models can predict the spatial dynamics of swimming cells, we have made many simplifications, some of which we now highlight as possible future directions of study. In this paper, we have demonstrated that, for non-spherical cells, rapid advection between regions of differing strain can generate variability between the IBM and population-level model. Likewise, time-varying shear is also expected to generate variability. Further analysis investigating the combined effect of non-sphericity and gyrotaxis is therefore desirable. For example Manela & Frankel (2003) found exceptional dispersion rates which were unique to non-spherical cells, and so it would be informative to explore the implications of this in terms of the spatial distribution of cells in the flow fields considered in this paper. Swimming micro-organisms display a range of behaviours, for example ‘run-and-tumble’ or ‘run-and-reverse’ swimming motions. Luchsinger, Bergesen & Mitchell (1999) demonstrated that the optimal swimming strategy can

depend on the fluid motions and so, as generalized Taylor dispersion can be naturally extended to alternative swimming strategies (Bearon 2003), it may be of interest to explore how different swimming strategies affect the spatial dispersion. We highlighted the importance of boundary conditions for determining the spatial distribution, yet in the IBM we only considered simple reflection of swimming cells which encounter a boundary. Extending the IBM to incorporate recent work integrating detailed experimental data and mathematical models on the behaviour of swimming micro-organisms near boundaries (e.g. Cisneros *et al.* 2008) could be worthwhile. Additionally, it would be interesting to understand how to incorporate such an individual-based model into appropriate boundary conditions of the population-level model.

Throughout this work, we have neglected any coupling between cells. Even at low volume fractions, cells can interact via the hydrodynamics, for example bioconvection has been successfully modelled by coupling the Navier–Stokes equations, with density being dependent on the concentration of cells, to a population-level model for the cell concentration. It would be interesting to explore whether the full population-level model used in this paper based on the generalized Taylor dispersion model gives any different predictions for bioconvection. The two-dimensional model of a convection cell without hydrodynamical interactions presented in this paper displayed a peak in cell concentration near the top-left corner, which, if not artefactual, may cause interesting features in models of bioconvection when the cell concentration is coupled to the hydrodynamics. Of further complexity is to include the direct cell–cell hydrodynamic coupling, which for self-propelled cells at high volume fractions has been shown to drive fluid motions on spatial and temporal scales much larger than the individual cells (Cisneros *et al.* 2007).

Supplementary material is available at journals.cambridge.org/flm.

## Appendix. Calculation of mean-swimming and diffusion

### A.1. *No flow*

We first consider the solution in the absence of flow, $Pr = 0$, taking $f = f^{(0)}$ and $\boldsymbol{b} = \boldsymbol{b}^{(0)}$. Setting $Pr = 0$ in the governing equations for $f$, (2.4), (2.10), subject to the appropriate integral constraint, (2.12), we obtain the von Mises equilibrium orientation distribution

$$f^{(0)} = \frac{1}{2\pi I_0(\kappa)} \exp(\kappa \cos\theta), \tag{A 1}$$

where the normalization constant is $I_0(\kappa) = (1/(2\pi)) \int_0^{2\pi} \exp(\kappa \cos\theta)\, \mathrm{d}\theta$, the modified Bessel function of the first kind and zero order (e.g. see Batschelet 1981). This results in the following expression for the mean-swimming direction:

$$\overline{p_x} = 0, \quad \overline{p_y} = \frac{I_1(\kappa)}{I_0(\kappa)}, \tag{A 2}$$

where $I_1(\kappa) = (1/(2\pi)) \int_0^{2\pi} \cos\theta \exp(\kappa \cos\theta)\, \mathrm{d}\theta$ is the modified Bessel function of the first kind and first order.

General expressions for the vector $\boldsymbol{b}^{(0)}$ and leading order expressions for the diffusion tensor are quite complicated, but the $\boldsymbol{x}$ components can be found as fairly simple

functions of $\kappa$. On integrating (2.11) with $Pr = 0$ with respect to $\theta$, we obtain

$$\kappa \sin\theta b_x^{(0)} + \frac{\mathrm{d}b_x^{(0)}}{\mathrm{d}\theta} = \frac{1}{2\pi\kappa I_0(\kappa)}(\exp(\kappa\cos\theta) - C_1), \tag{A 3}$$

where $C_1$ is a constant to be determined. Integrating again, gives the following expression for $b_x$:

$$b_x^{(0)} = \frac{\exp(\kappa\cos\theta)}{2\pi\kappa I_0(\kappa)}\left(\theta - C_1\int_0^{\theta}\exp(-\kappa\cos\theta')\theta' - C_2\right). \tag{A 4}$$

In order for $b_x^{(0)}$ to be a periodic function, and noting that $I_0(\kappa) = I_0(-\kappa)$, we find that $C_1 = 1/I_0(\kappa)$. Integrating (A 3) over all $\theta$ gives an easy way to compute the leading order $D_{xx}$ component of the non-dimensional diffusion tensor:

$$D_{xx} = \int_0^{2\pi} b_x p_x \,\mathrm{d}\theta = \int_0^{2\pi} b_x \sin\theta \,\mathrm{d}\theta = \frac{1}{\kappa^2}\left(1 - \frac{1}{I_0(\kappa)^2}\right). \tag{A 5}$$

The dimensional components are obtained via multiplication by $v_s^2/d_r$.

This agrees with the ad-hoc dimensional expression for $D_{xx} = v_s^2\tau\,\mathrm{var}(p_x)$ proposed by Pedley & Kessler (1990) if we take the correct correlation time. We can compute

$$\mathrm{var}(p_x) = \int_0^{2\pi} f^{(0)} p_x^2 \,\mathrm{d}\theta = \frac{1}{2}\left(1 - \frac{I_2(\kappa)}{I_0(\kappa)}\right), \tag{A 6}$$

and hence we should take the correlation time as

$$\tau = \frac{1}{d_r}\frac{2\left(1 - \dfrac{1}{I_0(\kappa)^2}\right)}{\kappa^2\left(1 - \dfrac{I_2(\kappa)}{I_0(\kappa)}\right)}. \tag{A 7}$$

Thus, the correlation time is inversely proportional to the rotary diffusion coefficient, $d_r$, and monotonically decreases as a function of $\kappa$, the bias due to gravitaxis.

Furthermore, if we compute $D_{yy} = v_s^2\tau\,\mathrm{var}(p_y)$ using this correlation time, specifically, we can compute

$$\mathrm{var}(p_y) = \int_0^{2\pi} f^{(0)}(p_y - \overline{p_y})^2 \,\mathrm{d}\theta = \frac{1}{2}\left(1 + \frac{I_2(\kappa)}{I_0(\kappa)} - 2\left(\frac{I_1(\kappa)}{I_0(\kappa)}\right)^2\right), \tag{A 8}$$

and using the expression for $\tau$ from (A 7), the diffusion tensor shows very good agreement.

### A.2. *Weak flow*

For weak flow, $Pr \ll 1$, consider the following perturbation expansion for $f$ and $\boldsymbol{b}$:

$$f = f^{(0)} + Prf^{(1)} + O(Pr^2), \tag{A 9}$$

$$\boldsymbol{b} = \boldsymbol{b}^{(0)} + Pr\boldsymbol{b}^{(1)} + O(Pr^2). \tag{A 10}$$

If we insert this expansion into the governing equations for $f$, (2.4), (2.10), subject to the appropriate integral constraint, (2.12), we obtain at leading order the distribution found in the no-flow case. At $O(Pr)$, we obtain the following expression for $f^{(1)}$:

$$f^{(1)} = \frac{\exp(\kappa\cos\theta)}{4\pi I_0(\kappa)}\Bigg( -\hat{\omega}\theta + \alpha_0(-\hat{E}_{11}(\cos 2\theta - 1) + \hat{E}_{12}\sin 2\theta) + \frac{\hat{\omega}}{I_0(\kappa)}\int_0^\theta \exp(-\kappa\cos\theta')\theta' - C_3\Bigg). \quad (A\,11)$$

As for the leading order calculation of $D_{xx}$, we can integrate an equation equivalent to (A 3) for $f^{(1)}$ to obtain the $x$ component of the mean-swimming direction

$$\overline{p}_x = Pr\int_0^{2\pi} f^{(1)}\sin\theta\,\mathrm{d}\theta = \frac{Pr}{\kappa}\left(\frac{\hat{\omega}}{2}\left(\frac{1}{I_0(\kappa)^2} - 1\right) + \alpha_0\hat{E}_{12}\frac{I_2(\kappa)}{I_0(\kappa)}\right). \quad (A\,12)$$

For vertical Couette flow, $\hat{\boldsymbol{V}} = x\boldsymbol{j}$, considered in § 3.2, we have that $\hat{\omega} = 1$, $\hat{E}_{12} = 1/2$, and thus

$$\overline{p}_x = \frac{Pr}{2\kappa}\left(\frac{1}{I_0(\kappa)^2} - 1 + \alpha_0\frac{I_2(\kappa)}{I_0(\kappa)}\right). \quad (A\,13)$$

### A.3. *Large Pr limit*

From (2.4) and (2.10), we have that the equilibrium orientation distribution, $f$, satisfies

$$Pr\frac{\mathrm{d}}{\mathrm{d}\theta}\left(\left(\frac{1}{2}\hat{\omega} - \alpha_0(\sin(2\theta)\hat{E}_{11} + \cos(2\theta)\hat{E}_{12})\right)f\right) = -\frac{\mathrm{d}}{\mathrm{d}\theta}\left(\kappa\sin\theta f + \frac{\mathrm{d}f}{\mathrm{d}\theta}\right). \quad (A\,14)$$

For large $Pr$, consider the following perturbation expansion for $f$:

$$f = \frac{1}{2\pi}\left(f^{(0)} + \frac{1}{Pr}f^{(1)} + \left(\frac{1}{Pr}\right)^2 f^{(2)} + \dots\right), \quad (A\,15)$$

which yields at leading order in $Pr$

$$f^{(0)} = \frac{C_0}{\frac{1}{2}\hat{\omega} - \alpha_0(\sin(2\theta)\hat{E}_{11} + \cos(2\theta)\hat{E}_{12})}, \quad (A\,16)$$

where $C_0$ is a normalization constant which ensures that $f^{(0)}$ satisfies the constraint (2.12). This expression is valid provided the straining motion is not sufficiently strong to generate a singularity in the expression. For example, for vertical Couette flow, with $\hat{\omega} = 1$, $\hat{E}_{11} = 0$, $\hat{E}_{12} = 1/2$, we require that $\alpha_0 < 1$. Using symmetry arguments, we have zero mean-swimming at leading order, $\overline{\boldsymbol{p}}^{(0)} = \int_0^{2\pi} f^{(0)}\boldsymbol{p}\,\mathrm{d}\theta = \boldsymbol{0}$.

The following expression for $f^{(1)}$ follows on integrating (A 14):

$$f^{(1)} = -\frac{f^{(0)}}{C_0}\left(\kappa\sin\theta f^{(0)} + \frac{\mathrm{d}f^{(0)}}{\mathrm{d}\theta} + C_1\right), \quad (A\,17)$$

where $C_1 = 0$ is a normalization constant which ensures that $f^{(1)}$ integrates to zero. Using symmetry arguments, we are thus able to compute the mean-swimming to $O(1/Pr)$:

$$\overline{\boldsymbol{p}} = \frac{1}{2\pi Pr}\int_0^{2\pi} f^{(1)}\boldsymbol{p}\,\mathrm{d}\theta = -\frac{\kappa}{2\pi C_0 Pr}\int_0^{2\pi}(f^{(0)})^2\sin\theta\,\boldsymbol{p}\,\mathrm{d}\theta. \quad (A\,18)$$

We consider the following perturbation expansion for $\boldsymbol{b}$:

$$\boldsymbol{b} = \frac{1}{2\pi}\left(\frac{1}{Pr}\boldsymbol{b}^{(1)} + \left(\frac{1}{Pr}\right)^2\boldsymbol{b}^{(2)} + \cdots\right). \quad (A\,19)$$

From (2.4) and (2.11), and making use of the leading order expression for $f$, we have that $\boldsymbol{b}$ satisfies:

$$Pr\left(-\frac{\mathrm{d}}{\mathrm{d}\theta}\left(\frac{C_0}{f^{(0)}}\boldsymbol{b}\right)-\boldsymbol{b}\cdot\hat{\mathbf{G}}\right)=f(\boldsymbol{p}-\overline{\boldsymbol{p}})+\frac{\mathrm{d}}{\mathrm{d}\theta}\left(\kappa\sin\theta\boldsymbol{b}+\frac{\mathrm{d}\boldsymbol{b}}{\mathrm{d}\theta}\right), \tag{A 20}$$

subject to the integral constraint (2.12).

At leading order, we thus obtain the following equation for $\boldsymbol{b}^{(1)}$:

$$-\frac{\mathrm{d}}{\mathrm{d}\theta}\left(\frac{C_0}{f^{(0)}}\boldsymbol{b}^{(1)}\right)-\boldsymbol{b}^{(1)}\cdot\hat{\mathbf{G}}=f^{(0)}\boldsymbol{p}. \tag{A 21}$$

This will be solved explicitly below for two classes of problems: spherical cells in arbitrary flow; and non-spherical cells in vertical Couette flow.

To calculate the diffusion tensor, by combining (2.9) and (2.11), we can rewrite the diffusion tensor as

$$\boldsymbol{D}=\int_0^{2\pi}\left[\frac{\boldsymbol{b}}{f}\mathscr{L}\boldsymbol{b}\right]^{sym}\mathrm{d}\theta. \tag{A 22}$$

Writing in this form is particularly convenient for calculating the leading order expression for the diffusion tensor as it only requires calculation of $\boldsymbol{b}^{(1)}$ and not higher order terms.

At $O(1/Pr)$, we see that the diffusion tensor is zero

$$\boldsymbol{D}=-\frac{C_0}{2\pi}\int_0^{2\pi}\left[\frac{\boldsymbol{b}^{(1)}}{f^{(0)}}\frac{\mathrm{d}}{\mathrm{d}\theta}\left(\frac{\boldsymbol{b}^{(1)}}{f^{(0)}}\right)\right]^{sym}\mathrm{d}\theta=\mathbf{0}. \tag{A 23}$$

At $O(1/Pr^2)$, we can write the diffusion tensor as

$$\boldsymbol{D}=\frac{1}{2\pi Pr^2}\int_0^{2\pi}\left[\frac{f^{(1)}}{(f^{(0)})^2}\boldsymbol{b}^{(1)}\frac{\mathrm{d}}{\mathrm{d}\theta}\left(\frac{C_0\boldsymbol{b}^{(1)}}{f^{(0)}}\right)-\frac{\boldsymbol{b}^{(1)}}{f^{(0)}}\frac{\mathrm{d}}{\mathrm{d}\theta}\left(\kappa\sin\theta\boldsymbol{b}^{(1)}+\frac{\mathrm{d}\boldsymbol{b}^{(1)}}{\mathrm{d}\theta}\right)\right]^{sym}\mathrm{d}\theta. \tag{A 24}$$

This expression can be simplified, making use of the expression for $f^{(1)}$ from (A 17), to demonstrate explicitly that to $O(1/Pr^2)$ the diffusion tensor is independent of the gyrotactic bias

$$\boldsymbol{D}=\frac{1}{2\pi Pr^2}\int_0^{2\pi}\left[\left(\frac{\mathrm{d}}{\mathrm{d}\theta}\left(\frac{\boldsymbol{b}^{(1)}}{f^{(0)}}\right)\right)^2 f^{(0)}\right]^{sym}\mathrm{d}\theta. \tag{A 25}$$

A.3.1. *Spherical cells*

For spherical cells, $\alpha_0=0$, the leading order equilibrium orientation is $f^{(0)}=1$, and the constant $C_0=\hat{\omega}/2$. We can also explicitly compute higher order terms in the expansion:

$$f_1=-\frac{2\kappa}{\hat{\omega}}\sin\theta,\quad f_2=-\frac{2\kappa^2}{\hat{\omega}^2}\cos 2\theta+\frac{4k}{\hat{\omega}^2}\cos\theta. \tag{A 26}$$

We note that if $(\kappa/\hat{\omega})=O(Pr)$, i.e. the bias is very strong, or the vorticity is very close to zero, the expansion will fail. Hence, the leading order asymptotic expressions for the mean orientation are given by

$$\overline{p}_x=-\frac{\kappa}{\hat{\omega}Pr},\quad \overline{p}_y=\frac{2\kappa}{\hat{\omega}^2Pr^2}. \tag{A 27}$$

From (A 25), we obtain the following expression for the diffusion tensor:

$$\boldsymbol{D} = \frac{1}{2\pi Pr^2}\int_0^{2\pi}\left[\left(\frac{\mathrm{d}\boldsymbol{b}^{(1)}}{\mathrm{d}\theta}\right)^2\right]^{sym}\mathrm{d}\theta, \tag{A 28}$$

where (A 21) for $\boldsymbol{b}^{(1)}$ reduces to

$$-\frac{\mathrm{d}}{\mathrm{d}\theta}\left(\frac{\hat{\omega}}{2}\boldsymbol{b}^{(1)}\right) - \boldsymbol{b}^{(1)}\cdot\hat{\mathbf{G}} = \boldsymbol{p}, \tag{A 29}$$

which has solution $\boldsymbol{b}^{(1)} = \boldsymbol{\lambda}\cos\theta + \boldsymbol{\mu}\sin\theta$, where $\boldsymbol{\lambda}$ and $\boldsymbol{\mu}$ depend on the choice of $\hat{\mathbf{G}}$.

For example, for the flow given by (2.13), the diffusion tensor is given at leading order by

$$\boldsymbol{D} = \frac{1}{Pr^2(\alpha+1)^4}\begin{pmatrix} 2(\alpha-3)^2 & 0 \\ 0 & 2(3\alpha-1)^2 \end{pmatrix}. \tag{A 30}$$

Note that the expansion fails when $(\alpha+1)^2 = O(1/Pr)$, i.e. as we approach pure rotation, i.e. $\alpha = -1$.

With reference to § 3.1 on horizontal Couette flow, we therefore have the asymptotic result in the strong flow limit for homogeneous unidirectional shear flow, $\alpha = 0$, with $\hat{\omega} = 1$ as

$$\overline{p}_y = \frac{2\kappa}{Pr^2}, \quad D_{yy} = \frac{2}{Pr^2}. \tag{A 31}$$

A.3.2. *Axi-symmetric cells in vertical Couette flow*

For vertical Couette flow, $\hat{\boldsymbol{V}} = x\boldsymbol{j}$, considered in § 3.2, we have that $\hat{\omega} = 1$, $\hat{E}_{11} = 0$, $\hat{E}_{12} = \frac{1}{2}$, and thus from (A 16), we obtain the leading order equilibrium orientation

$$f^{(0)} = \frac{C_0}{\frac{1}{2} - \alpha_0\cos(2\theta)\hat{E}_{12}}, \tag{A 32}$$

and hence from (A 18) the leading order expression for mean horizontal swimming

$$\overline{p}_x = -\frac{\kappa}{Pr(1+\alpha_0)}. \tag{A 33}$$

Noting that $\boldsymbol{b}\cdot\hat{\mathbf{G}} = b_x\boldsymbol{j}$ for vertical Couette flow, (A 21), yields the following equation for $b_x^{(1)}$:

$$-\frac{\mathrm{d}}{\mathrm{d}\theta}\left(\frac{C_0}{f^{(0)}}b_x^{(1)}\right) = f^{(0)}\sin\theta, \tag{A 34}$$

which can be inserted into (A 25) to obtain the following leading order expression for $D_{xx}$, the component of the diffusion tensor required in § 3.2:

$$\begin{aligned} D_{xx} &= \frac{1}{2\pi C_0^2 Pr^2}\int_0^{2\pi}(f^{(0)})^3\sin^2\theta\,\mathrm{d}\theta \\ &= \frac{2-\alpha_0}{Pr^2(1-\alpha_0)(1+\alpha_0)^2}. \end{aligned} \tag{A 35}$$

### A.4. *Garlekin's method for general flow*

To calculate the mean-swimming direction and diffusion tensor for general flow, we make the following Fourier series expansion for $f$ and $\boldsymbol{b}$:

$$f = \frac{1}{2\pi}\left(1 + \sum_1^\infty a_k \cos k\theta + b_k \sin k\theta\right), \tag{A 36}$$

$$\boldsymbol{b} = \frac{1}{2\pi}\sum_1^\infty \boldsymbol{\lambda}_k \cos k\theta + \boldsymbol{\mu}_k \sin k\theta. \tag{A 37}$$

This expansion gives the following form for the mean-swimming direction and diffusion tensor:

$$\overline{\boldsymbol{p}} = \frac{1}{2}(b_1, a_1) \tag{A 38}$$

$$D_{xx} = \frac{1}{2}\mu_1^x + Pr\int_0^{2\pi} \frac{b^x(b^x\hat{G}_{xx} + b^y\hat{G}_{yx})}{f(\theta)}\,\mathrm{d}\theta, \tag{A 39}$$

$$D_{yy} = \frac{1}{2}\lambda_1^y + Pr\int_0^{2\pi} \frac{b^y(b^x\hat{G}_{xy} + b^y\hat{G}_{yy})}{f(\theta)}\,\mathrm{d}\theta, \tag{A 40}$$

$$D_{yx} = D_{xy} = \frac{1}{4}\left(\lambda_1^x + \mu_1^y\right) + \frac{Pr}{2}\int_0^{2\pi} \frac{(b^x(b^x\hat{G}_{xy} + b^y\hat{G}_{yy})) + (b^y(b^x\hat{G}_{xx} + b^y\hat{G}_{yx}))}{f(\theta)}\,\mathrm{d}\theta. \tag{A 41}$$

The Fourier coefficients of $f$ satisfy the following system of linear equations

$$\begin{aligned}\mathscr{L}f = {} & \frac{Pr}{2}\hat{\omega}\sum_1^\infty ka_k \sin k\theta - kb_k \cos k\theta \\ & -\frac{Pr}{2}\alpha_0\hat{E}_{11}\left(-a_1\cos\theta + b_1\sin\theta + \sum_1^\infty k(a_{k+2} - a_{k-2})\cos k\theta + k(b_{k+2} - b_{k-2})\sin k\theta\right) \\ & -\frac{Pr}{2}\alpha_0\hat{E}_{12}\left(a_1\sin\theta + b_1\cos\theta + \sum_1^\infty k(a_{k+2} + a_{k-2})\sin k\theta - k(b_{k+2} + b_{k-2})\cos k\theta\right) \\ & +\frac{\kappa}{2}\sum_1^\infty k(a_{k+1} - a_{k-1})\cos k\theta + k(b_{k+1} - b_{k-1})\sin k\theta \\ & +\sum_1^\infty k^2(a_k\cos k\theta + b_k\sin k\theta) = 0.\end{aligned} \tag{A 42}$$

Likewise, we can obtain a similar expression for the Fourier coefficients of $\boldsymbol{b}$:

$$\mathscr{L}\boldsymbol{b} - Pr\sum_1^\infty (\boldsymbol{\lambda}_k\cos k\theta + \boldsymbol{\mu}_k\sin k\theta)\cdot\hat{\mathbf{G}} = 2\pi f(\theta)(\boldsymbol{p} - \overline{\boldsymbol{p}}). \tag{A 43}$$

By truncating the infinite system of equations at $k = N$, the Fourier coefficients can be computed and hence the mean-swimming and diffusion tensor can be found. In practice we took $N = 10$ in our calculations as this gave sufficiently converged results.

A.4.1. *Spherical cells with no gyrotactic bias*

This analysis simplifies in the case of spherical cells where there is no bias, that is $\alpha_0 = 0, \kappa = 0$. In this case, the equilibrium distribution of orientation is uniform, $f(\theta) = 1/2\pi$, the mean-swimming direction is zero and only the $k = 1$ modes appear in the calculation of $\boldsymbol{b}$, i.e. we can let $\boldsymbol{b} = (1/(2\pi))(\boldsymbol{\lambda}\cos\theta + \boldsymbol{\mu}\sin\theta)$. We can further simplify the calculations by choosing co-ordinates such that the most general homogeneous shear is given by (2.13). In this case, the diffusion tensor is given by

$$D_{xx} = \frac{1}{2}\mu_x + \frac{Pr}{2}(\lambda_x\lambda_y + \mu_x\mu_y), \tag{A 44}$$

$$D_{yy} = \frac{1}{2}\lambda_y + \frac{Pr}{2}\alpha(\lambda_x\lambda_y + \mu_x\mu_y), \tag{A 45}$$

$$D_{yx} = D_{xy} = \frac{1}{4}(\lambda_x + \mu_y) + \frac{Pr}{4}\left((\lambda_x^2 + \mu_x^2)\alpha + (\lambda_y^2 + \mu_y^2)\right), \tag{A 46}$$

where the $\boldsymbol{\lambda}$ and $\boldsymbol{\mu}$ satisfy

$$-\frac{Pr}{2}(\alpha - 1)\mu_x + \lambda_x - Pr\lambda_y = 0, \tag{A 47}$$

$$\frac{Pr}{2}(\alpha - 1)\lambda_x + \mu_x - Pr\mu_y = 1, \tag{A 48}$$

$$-\frac{Pr}{2}(\alpha - 1)\mu_y + \lambda_y - Pr\alpha\lambda_x = 1, \tag{A 49}$$

$$\frac{Pr}{2}(\alpha - 1)\lambda_y + \mu_y - Pr\alpha\mu_x = 0. \tag{A 50}$$

This system of equations has two special features worth highlighting. Firstly, there is a singularity for pure strain, $\alpha = 1$, at $Pr = 1$. Secondly, for pure rotation, $\alpha = -1$, the solution is $\lambda_x = 0, \lambda_y = 1, \mu_x = 1, \mu_y = 0$ so that the diffusion tensor is isotropic and unaltered by the vorticity. Note that this agrees with the observation in § A.3, where we found that when $\alpha = -1$ the large $Pr$ asymptotic scaling for the diffusion tensor, $1/Pr^2$, failed.

## REFERENCES


Almog, Y. & Frankel, I. 1998 Rheology of dilute suspensions of Brownian dipolar axisymmetric particles. *J. Fluid. Mech.* **366**, 289–310.

Batschelet, E. 1981 *Circular Statistics in Biology*. Academic.

Bearon, R. N. 2003 An extension of generalized Taylor dispersion in unbounded homogeneous shear flows to run-and-tumble chemotactic bacteria. *Phys. Fluids* **15** (6), 1552–1563.

Bearon, R. N. & Grünbaum, D. 2008 From individual behaviour to population models: A case study using swimming algae. *J. Theor. Biol.* **251** (4), 679–697.

Bearon, R. N., Grünbaum, D. & Cattolico, R. A. 2006 Effects of salinity structure on swimming behavior and harmful algal bloom formation in *Heterosigma akashiwo*, a toxic raphidophyte. *Mar. Ecol. Prog. Ser.* **306**, 153–163.

Bees, M. A. & Croze, O. A. 2010 Dispersion of biased swimming micro-organisms in a fluid flowing through a tube. *Proc. R. Soc. Lond.* B **466** (2119), 2057–2077.

Bees, M. A., Hill, N. A. & Pedley, T. J. 1998 Analytical approximations for the orientation distribution of small dipolar particles in steady shear flows. *J. Math. Biol.* **36** (3), 269–298.

Birch, D. A., Young, W. R. & Franks, P. J. S. 2008 Thin layers of plankton: Formation by shear and death by diffusion. *Deep-Sea Res. Part 1* **55** (3), 277–295.

Brenner, H. 1979 Taylor dispersion in systems of sedimenting nonspherical Brownian particles 1. Homogeneous, centrosymmetric, axisymmetric particles. *J. Colloid Interface Sci.* **71** (2), 189–208.

Cisneros, L. H., Cortez, R., Dombrowski, C., Goldstein, R. E. & Kessler, J. O. 2007 Fluid dynamics of self-propelled microorganisms, from individuals to concentrated populations. *Exp. Fluids* **43** (5), 737–753.

Cisneros, L. H., Kessler, J. O., Ortiz, R., Cortez, R. & Bees, M. A. 2008 Unexpected bipolar flagellar arrangements and long-range flows driven by bacteria near solid boundaries. *Phys. Rev. Lett.* **101** (16), 168102.

Demkowicz, L., Oden, J. T., Rachowicz, W. & Hardy, O. 1989 Toward a universal h-p adaptive finite element strategy, Part 1. Constrained approximation and data structure. *Comput. Meth. Appl. Mech. Engng* **77**, 79–112.

Demmel, J. W., Eisenstat, S. C., Gilbert, J. R., Li, X. S. & Liu, J. W. H. 1999 A supernodal approach to sparse partial pivoting. *SIAM J. Matrix Anal. Applics.* **20**, 720–755.

Durham, W. M., Kessler, J. O. & Stocker, R. 2009 Disruption of vertical motility by shear triggers formation of thin phytoplankton layers. *Science* **323** (5917), 1067–1070.

Ferreira de Sousa, P. J. S. A. & Pereira, J. C. F. 2009 Dynamics of passive scalars and tracers advected by a two-dimensional tripolar vortex. *J. Fluid Mech.* **634**, 41–60.

Frankel, I. & Brenner, H. 1989 On the foundations of generalized Taylor dispersion theory. *J. Fluid Mech.* **204**, 97–119.

Frankel, I. & Brenner, H. 1991 Generalized Taylor dispersion phenomena in unbounded homogeneous shear flows. *J. Fluid Mech.* **230**, 147–181.

Frankel, I. & Brenner, H. 1993 Taylor dispersion of orientable Brownian particles in unbounded homogeneous shear flows. *J. Fluid Mech.* **255**, 129–156.

Franks, P. J. S. 1995 Coupled physical–biological models in oceanography. *Rev. Geophys.* **33**, 1177–1187.

Ghorai, S. & Hill, N. A. 1999 Development and stability of gyrotactic plumes in bioconvection. *J. Fluid Mech.* **400**, 1–31.

Heil, M. & Hazel, A. L. 2006 `oomph-lib` – An object-oriented multi-physics finite-element library in fluid structure interaction. In *Lecture Notes on Computational Science and Engineering* (ed. M. Schafer & H.-J. Bungartz), pp. 19–49. Springer.

Hill, N. A. & Bees, M. A. 2002 Taylor dispersion of gyrotactic swimming micro-organisms in a linear flow. *Phys. Fluids* **14** (8), 2598–2605.

Hill, N. A. & Häder, D. P. 1997 A biased random walk model for the trajectories of swimming micro-organisms. *J. Theor. Biol.* **186** (4), 503–526.

Hill, N. A. & Pedley, T. J. 2005 Bioconvection. *Fluid Dyn. Res.* **37** (1–2), 1–20.

Horner, R. A., Garrison, D. L. & Plumley, F. G. 1997 Harmful algal blooms and red tide problems on the US west coast. *Limnol. Oceanogr.* **42** (5), 1076–1088.

Ishikawa, T. 2009 Suspension biomechanics of swimming microbes. *J. R. Soc. Interface* **6** (39), 815–834.

Kessler, J. O. 1985 Hydrodynamic focusing of motile algal cells. *Nature* **313** (5999), 218–220.

Kim, S. & Karrila, S. J. 2005 *Microhydrodynamics: Principles and Selected Applications*. Dover.

Luchsinger, R., Bergesen, B. & Mitchell, J. G. 1999 Bacteria swimming strategies and turbulence. *Biophys. J.* **77**, 2377–2386.

Manela, A. & Frankel, I. 2003 Generalized Taylor dispersion in suspensions of gyrotactic swimming micro-organisms. *J. Fluid Mech.* **490**, 99–127.

McManus, M. A., Alldredge, A. L., Barnard, A. H., Boss, E., Case, J. F., Cowles, T. J., Donaghay, P. L., Eisner, L. B., Gifford, D. J., Greenlaw, C. F., Herren, C. M., Holliday, D. V., Johnson, D., MacIntyre, S., McGehee, D. M., Osborn, T. R., Perry, M. J., Pieper, R. E., Rines, J. E. B., Smith, D. C., Sullivan, J. M., Talbot, M. K., Twardowski, M. S., Weidemann, A. & Zaneveld, J. R. 2003 Characteristics, distribution and persistence of thin layers over a 48 hour period. *Mar. Ecol. Prog. Ser.* **261**, 1–19.

Morris, J. F. & Brady, J. F. 1996 Self-diffusion in sheared suspensions. *J. Fluid Mech.* **312**, 232–252.

Ottino, J. M. 1990 Mixing, chaotic advection, and turbulence. *Annu. Rev. Fluid Mech.* **22**, 207–253.

Pedley, T. J. & Kessler, J. O. 1990 A new continuum model for suspensions of gyrotactic microorganisms. *J. Fluid Mech.* **212**, 155–182.

Pedley, T. J. & Kessler, J. O. 1992 Hydrodynamic phenomena in suspensions of swimming microorganisms. *Annu. Rev. Fluid Mech.* **24**, 313–358.

Raven, J. A. & Falkowski, P. G. 1999 Oceanic sinks for atmospheric CO2. *Plant Cell. Environ.* **22** (6), 741–755.

Sharples, J., Moore, C. M., Rippeth, T. P., Holligan, P. M., Hydes, D. J., Fisher, N. R. & Simpson, J. H. 2001 Phytoplankton distribution and survival in the thermocline. *Limnol. Oceanogr.* **46** (3), 486–496.

Sobczyk, K. 1991 *Stochastic Differential Equations: With Applications to Physics and Engineering*. Kluwer.

Steinbuck, J. V., Stacey, M. T., McManus, M. A., Cheriton, O. M. & Ryan, J. P. 2009 Observations of turbulent mixing in a phytoplankton thin layer: Implications for formation, maintenance, and breakdown. *Limnol. Oceanogr.* **54** (4), 1353–1368.

Thorn, G. J. & Bearon, R. N. 2010 Transport of gyrotactic organisms in general 3D flow fields. *Phys. Fluids* **22** (4), 041902.

Torney, C. & Neufeld, Z. 2007 Transport and aggregation of self-propelled particles in fluid flows. *Phys. Rev. Lett.* **99** (7), 078101.

Warhaft, Z. 2000 Passive scalars in turbulent flows. *Annu. Rev. Fluid Mech.* **32**, 203–240.

Zienkiewicz, O. C. & Zhu, J. 1992*a* The superconvergent patch recovery and a posteriori error estimates. Part 1. The recovery technique. *Intl J. Numer. Meth. Engng* **33**, 1331–1364.

Zienkiewicz, O. C. & Zhu, J. 1992*b* The superconvergent patch recovery and a posteriori error estimates. Part 2: Error estimates and adaptivity. *Intl J. Numer. Meth. Engng* **33**, 1365–1382.